Journal of Computational Physics 499 (2024) 112704

Contents lists available at ScienceDirect

Journal of Computational Physics

journal homepage: www.elsevier.com/locate/jcp

Viscoelastic constitutive artificial neural networks (vCANNs) – A framework for data-driven anisotropic nonlinear finite viscoelasticity

Kian P. Abdolazizi [a], Kevin Linka [a], Christian J. Cyron [a,b,*]

[a] Institute for Continuum and Material Mechanics, Hamburg University of Technology, Eißendorfer Straße 42, 21073 Hamburg, Germany
[b] Institute of Material Systems Modeling, Helmholtz-Zentrum Hereon, Max-Planck-Straße 1, 21502 Geesthacht, Germany

ARTICLE INFO

Dataset link: https://github.com/ConstitutiveANN/vCANN

Keywords:
Nonlinear viscoelasticity
Deep learning
Data-driven mechanics
Physics-informed machine learning
Constitutive modeling
Soft materials

ABSTRACT

The constitutive behavior of polymeric materials is often modeled by finite linear viscoelastic (FLV) or quasi-linear viscoelastic (QLV) models. These popular models are simplifications that typically cannot accurately capture the nonlinear viscoelastic behavior of materials. For example, the success of attempts to capture strain (rate)-dependent behavior has been limited so far. To overcome this problem, we introduce viscoelastic Constitutive Artificial Neural Networks (vCANNs), a novel physics-informed machine learning framework for anisotropic nonlinear viscoelasticity at finite strains. vCANNs rely on the concept of generalized Maxwell models enhanced with nonlinear strain (rate)-dependent properties represented by neural networks. The flexibility of vCANNs enables them to automatically identify accurate and sparse constitutive models of a broad range of materials. To test vCANNs, we trained them on stress-strain data from Polyvinyl Butyral, the electro-active polymers VHB 4910 and 4905, and a biological tissue, the rectus abdominis muscle. Different loading conditions were considered, including relaxation tests, cyclic tension-compression tests, and blast loads. We demonstrate that vCANNs can learn to capture the behavior of all these materials accurately and computationally efficiently without human guidance. Our source code is available at https://github.com/ConstitutiveANN/vCANN.

1. Introduction

Many important materials, such as elastomers or soft biological tissues, undergo large deformations and exhibit nonlinear viscoelasticity behavior. Biological tissues additionally typically exhibit a pronounced anisotropy. Numerous experiments have confirmed that elastomers [1–3] and similarly ligaments and tendons exhibit nonlinear viscoelasticity [4–11]. In the past, many constitutive models have been proposed to characterize these materials. However, selecting an appropriate model and identifying its material parameters requires expert knowledge. Further, when selecting a model, one usually has to make a compromise between its computational efficiency and its ability to capture nonlinear viscoelasticity adequately. Therefore, this contribution aims to develop a data-driven framework that automatically discovers constitutive models for anisotropic nonlinear viscoelasticity at finite strains. Ideally, the framework is simple and numerically efficient but, at the same time, highly versatile, describing a wide range of materials. As a starting point for our development, we review existing modeling approaches and identify their advantages and limitations.

* Corresponding author at: Institute for Continuum and Material Mechanics, Hamburg University of Technology, Eißendorfer Straße 42, 21073 Hamburg, Germany.
E-mail address: christian.cyron@tuhh.de (C.J. Cyron).

https://doi.org/10.1016/j.jcp.2023.112704
Received 21 March 2023; Received in revised form 21 October 2023; Accepted 4 December 2023

Available online 7 December 2023
0021-9991/

Broadly, existing approaches to describe viscoelasticity can be categorized into hereditary integral and internal variables models. In hereditary integral models, the viscoelastic stress response is calculated by the convolution of the deformation history and an appropriate kernel function [12–14]. A potential difficulty of these models is that, in particular for multiple integral models, the experimental determination of the kernel functions can be cumbersome [15,16] and very sensitive to noise [17]. Also, the numerical implementation is often challenging since one must account - in general - for the whole deformation history. Therefore, hereditary models have mainly been applied to simple one-dimensional problems and have had only a limited impact on finite element (FE) analysis. An important exception is the theory of quasi-linear viscoelasticity (QLV) [18]. In QLV, the integrand of the hereditary integral is the product of a time-dependent reduced relaxation function and the rate of the instantaneous elastic stress, usually derived from a hyperelastic strain energy function. Often, the reduced relaxation function is represented by a Prony series [19]. Due to its computational efficiency and a large number of candidate functions for the reduced relaxation function and the instantaneous elastic stress, this approach has been used frequently [4,20–30]. Due to the linear relationship between the reduced relaxation function and the instantaneous elastic stress within the hereditary integral, QLV falls short of representing fully general nonlinear viscoelastic behavior. In fact, normalized relaxation curves predicted by QLV have the same shape, independent of the strain, which contradicts experimental observations.

Within the group of internal variable models, two model families have been particularly successful. The first family follows Simo [31] and assumes an additive split of the stress into an equilibrium part and n non-equilibrium overstresses, in analogy to the generalized Maxwell model. The number of overstresses is arbitrary and can be independently selected for isotropic and anisotropic contributions to the overall material behavior. Linear ordinary differential equations (ODEs) with constant coefficients govern the evolution of the overstresses, serving as internal variables. Closed-form solutions of the evolution equations by convolution integrals result in efficient time integration algorithms [32]. Therefore, these models appear in many commercial FE codes [33]. Due to the linear evolution equations, models of this family are theoretically restricted to finite linear viscoelasticity (FLV), i.e., finite strains but small perturbations away from the thermodynamic equilibrium. Although originating from different theories, FLV and QLV are similar [34,35]. Thus, FLV suffers from the same limitations as QLV, failing to represent general fully nonlinear viscoelastic behavior such as strain (rate)-dependent viscous properties. Peña et al. [36] and Calvo et al. [37] attempted to account for nonlinear viscoelastic effects by choosing strain-dependent coefficients of the evolution equation. These attempts led to improved but still not yet fully satisfactory results. FLV models have, for example, been employed in [37–42]. The second model family describes finite nonlinear viscoelasticity (FNLV), i.e., finite strains and finite perturbations away from the thermodynamic equilibrium [43]. Motivated by the decomposition of the strain into an elastic and viscous part in the theory of linear viscoelasticity, FNLV models are based on the multiplicative decomposition of the deformation gradient into an elastic and viscous part proposed by [44]. In general, nonlinear ODEs govern the evolution of the viscous part of the deformation gradient, serving as an internal variable. In analogy to the generalized Maxwell model, multiple decompositions of the deformation gradient are possible, each associated with the non-equilibrium stress of a Maxwell element [43] and an associated internal variable (representing a viscous part of the deformation gradient). Applications are documented for rubber [1,2,33,45–47] and soft biological tissues [48–54]. The drawbacks of FNLV models are the computational cost, especially for large-scale simulations, and their limited availability in widely used commercial FE software.

The above models have been developed by specialists, and also the selection and calibration of these models for a specific material typically require some expert knowledge. Data-driven modeling approaches such as machine learning circumvent these problems by providing a flexible computational framework that directly infers constitutive relations from data rather than specifying them a priori [55–60]. In deep learning, modeling the time-history effects of viscoelasticity requires an artificial neural network (ANN) for temporal signal processing. Therefore, recurrent neural networks (RNNs) and similar architectures, usually employed for speech recognition or time series prediction, have been used intensively. Oeser and Freitag [61] used an Elman network to model materials with fading memory based on fractional differential equations under cyclic loading conditions. Instead of a material model, [62] applied RNNs to fuzzy data to describe time-dependent material behavior within the finite element method. The inelastic material behavior of rubber-like materials was modeled with RNNs and used in FE simulations by [63]. Chen [64] modeled small-strain viscoelasticity using long short-term memory (LSTM). RNNs compute a material's stress state based on a time window comprising the strain states of n previous time steps. For FE simulations, this entails a significant increase in computational cost, as the strain states of the previous n time steps have to be stored for each quadrature point. In [64], LSTMs reacted sensitively to time step sizes and loading cases, deviating from those used during training. Moreover, the width of the time window directly affects the fading memory property [65] of the material and is difficult to determine. The thermo-viscoelastic constitutive behavior of polypropylene was modeled by [66] using a mechanistic/data-driven hybrid approach in which a neural network represented the viscous part of their rheological model. Marino et al. [67] employed full-field strain measurements to calibrate the material parameters of a generalized Maxwell model for isotropic linear viscoelasticity in the small-strain regime. Linka et al. [68] modeled the time-dependent behavior of human brain tissue by QLV. Therein, neural networks learned the constant relaxation coefficients and times of the reduced relaxation function. A purely data-driven approach to constitutive modeling, which does not require any explicit constitutive models but builds on material data only, was introduced by [69] and recently extended to inelastic materials [70,71]. However, this approach typically requires a large database to describe the material's mechanical behavior [72].

To overcome the limitations of the above-delineated approaches, at least in part, herein we propose viscoelastic Constitutive Artificial Neural Networks (vCANNs), a novel physics-informed machine learning framework for anisotropic nonlinear viscoelasticity at large strains. vCANNs are based on a generalized Maxwell model, enhanced with nonlinear strain (rate)-dependent relaxation coefficients and relaxation times represented by neural networks. We show that the data-driven nature of vCANNs enables them to identify accurate anisotropic nonlinear viscoelastic constitutive models automatically. The number of Maxwell elements adapts

automatically during the training, promoting a sparse model through L_1 regularization. Adopting the computationally very efficient framework of QLV and FLV, we leverage these well-established theories to model anisotropic nonlinear viscoelasticity. The achieved degree of accuracy is unmatched by similar traditional approaches that have been proposed. We trained vCANNs on stress-strain data from Polyvinyl Butyral, the electro-active polymers VHB 4910 and 4905, and the rectus abdominis muscle. Different loading conditions were considered, including relaxation tests, cyclic tension-compression tests, and blast loads. In all these cases, vCANNs were found to be able to learn the behavior of the materials within minutes, without human guidance, and with high accuracy.

2. Theory

In this section, we derive the theoretical framework of vCANNs. They can be considered an extension of CANNs, which were introduced in [72], to anisotropic nonlinear viscoelasticity. Therefore, we initially provide a brief review of CANNs. The section's central part will be devoted to the viscoelastic enhancement of CANNs.

2.1. Describing anisotropic hyperelasticity with generalized structural tensors

Many materials of interest exhibit direction-dependent, i.e., anisotropic, mechanical properties. CANNs provide a physics-informed machine learning framework for anisotropic hyperelasticity to describe these materials in a very general way. To this end, CANNs employ invariant theory, and the concept of generalized structural tensors [73]. A material is called hyperelastic if a strain energy function $\Psi = \Psi(\mathbf{F})$, depending only on the deformation gradient $\mathbf{F}$, can describe the material's mechanical behavior [74]. To fulfill the principle of objectivity [75], one usually represents Ψ in terms of the right Cauchy–Green tensor $\mathbf{C} = \mathbf{F}^{\mathrm{T}}\mathbf{F}$, i.e., $\Psi = \Psi(\mathbf{C})$. For an incompressible hyperelastic material ($\det \mathbf{C} = 1$), the instantaneous elastic 2nd Piola–Kirchhoff stress tensor is given by

$$\mathbf{S}^e = -p\mathbf{C}^{-1} + 2\frac{\partial \Psi}{\partial \mathbf{C}}, \tag{1}$$

where p is a Lagrangian multiplier ensuring incompressibility. The superscript $(\cdot)^e$ explicitly distinguishes the instantaneous elastic stress from the viscoelastic stress derived in the next paragraph. In Eq. (1), the first and second terms represent the volumetric and isochoric stress contribution, respectively. The treatment of compressible and nearly compressible materials is equally possible with our proposed framework of anisotropic nonlinear viscoelasticity. For brevity, and because finite-strain viscoelasticity plays a particularly prominent role in materials often modeled as (nearly) incompressible (such as rubber materials or biological tissues), we limit the discussion in the following to incompressible materials.

To describe the mechanical behavior of an anisotropic material, one can define several so-called preferred directions represented by unit direction vectors $\boldsymbol{l}_j \in \mathbb{R}^3$, $j = 1, 2, \dots, J$, and define the following $J + 1$ structural tensors

$$\mathbf{L}_0 = \frac{1}{3}\mathbf{I}, \quad \mathbf{L}_j = \boldsymbol{l}_j \otimes \boldsymbol{l}_j, \quad \left\|\boldsymbol{l}_j\right\| = 1, \quad j = 1, 2, \dots, J. \tag{2}$$

Here, $\mathbf{I}$ denotes the second-order identity tensor, and the associated $\mathbf{L}_0$ is used to describe the isotropic part of the material's constitutive behavior. The preferred directions $\boldsymbol{l}_j$ can often be interpreted as directions of fiber families embedded in the material. It can be shown that to preserve the material symmetry, the strain energy function Ψ has to be an isotropic function of the quantities $\mathbf{C}$ and $\mathbf{L}_j$, $j = 1, 2, \dots, J$ [76]. It can be shown [77,78] that this is the case if the strain energy function depends only on the following invariants:

$$\operatorname{tr}\mathbf{C}, \quad \operatorname{tr}\mathbf{C}^2, \quad \operatorname{tr}\mathbf{C}^3, \quad \operatorname{tr}\left(\mathbf{C}\mathbf{L}_j\right), \quad \operatorname{tr}\left(\mathbf{C}^2\mathbf{L}_j\right), \quad j = 1, 2, \dots, J, \tag{3}$$

$$\operatorname{tr}\left(\mathbf{C}\mathbf{L}_i\mathbf{L}_j\right), \quad \operatorname{tr}\left(\mathbf{L}_i\mathbf{L}_j\right), \quad \operatorname{tr}\left(\mathbf{L}_i\mathbf{L}_j\mathbf{L}_k\right), \quad 1 \le i < j < k \le J. \tag{4}$$

The latter two types of invariants in Eq. (4) are constant and can therefore be omitted from the arguments of Ψ. For practical applications, the influence of the first invariant type in Eq. (4) is usually negligible. Therefore, Ψ can commonly be expressed as

$$\Psi = \Psi\left(\operatorname{tr}\mathbf{C}, \operatorname{tr}\mathbf{C}^2, \operatorname{tr}\mathbf{C}^3, \operatorname{tr}\left(\mathbf{C}\mathbf{L}_1\right), \operatorname{tr}\left(\mathbf{C}^2\mathbf{L}_1\right), \dots, \operatorname{tr}\left(\mathbf{C}\mathbf{L}_J\right), \operatorname{tr}\left(\mathbf{C}^2\mathbf{L}_J,\right)\right). \tag{5}$$

With the $2R + 1$ generalized invariants

$$\tilde{I}_r = \operatorname{tr}\left(\mathbf{C}\tilde{\mathbf{L}}_r\right), \qquad \tilde{J}_r = \operatorname{tr}\left[(\det\mathbf{C})\mathbf{C}^{-\mathrm{T}}\tilde{\mathbf{L}}_r\right] = \operatorname{tr}\left[(\operatorname{cof}\mathbf{C})\tilde{\mathbf{L}}_r\right], \qquad \mathrm{III}_{\mathbf{C}} = \det\mathbf{C}, \qquad r = 1, 2, \dots, R, \tag{6}$$

relying on the R generalized structural tensors

$$\tilde{\mathbf{L}}_r = \sum_{j=0}^{J_R} w_{rj}\mathbf{L}_{rj}, \quad r = 1, 2, \dots, R, \tag{7}$$

where

$$\mathbf{L}_{r0} = \mathbf{L}_0, \quad \sum_{j=0}^{J_R} w_{rj} = 1, \quad w_{rj} \ge 0, \quad r = 1, 2, \dots, R, \tag{8}$$

and employing the short-hand notation

$$\tilde{\mathcal{I}} = \left\{ \tilde{I}_1, \tilde{J}_1, \dots, \tilde{I}_R, \tilde{J}_R, \mathrm{III}_{\mathbf{C}} \right\}, \tag{9}$$

we can alternatively express Eq. (5), according to [73], in the form

$$\Psi = \Psi\left(\tilde{\mathcal{I}}\right). \tag{10}$$

The generalized structural tensors represent convex combinations of the standard structural tensors $\mathbf{L}_{rj} = \boldsymbol{l}_{rj} \otimes \boldsymbol{l}_{rj}$ introduced in Eq. (2). We use a double index rj to emphasize that, in principle, each generalized structural tensor $\tilde{\mathbf{L}}_r$ can rely on a different subset of J_r preferred material directions $\boldsymbol{l}_{rj}, j = 1, \dots, J_r$.

To describe not only the stress-strain behavior of a material but also the dependence of this behavior on certain in general non-mechanical parameters, it is convenient to augment the arguments of Ψ with a feature vector $\mathbf{f} = [f_1, f_2, \cdots, f_{N_f}]^{\mathrm{T}}$, where N_f denotes the number of features. For example, $\mathbf{f}$ could carry information on the material's microstructure or production process. Thus,

$$\Psi = \Psi\left(\tilde{\mathcal{I}}, \mathbf{f}\right). \tag{11}$$

Apart from material symmetry and the principle of objectivity, the strain energy function has to fulfill several other conditions. The strain energy must always be positive, $\Psi \geq 0$. Also, the strain energy is required to approach infinity if the material is shrunk to zero or expanded to infinite volume, i.e., $\Psi \to \infty$ for $\det \mathbf{C} \to \infty$ or $\det \mathbf{C} \to 0^+$, which is called the growth condition. If a stress-free reference configuration is assumed, the strain energy function and the stress have to fulfill the normalization condition: $\Psi(\mathbf{C} = \mathbf{I}) = 0$ and $\mathbf{S}^e(\mathbf{C} = \mathbf{I}) = -p\mathbf{I} + 2\frac{\partial \Psi}{\partial \mathbf{C}}\Big|_{\mathbf{C}=\mathbf{I}} = \mathbf{0}$. In addition, the strain energy function may be desired to satisfy the polyconvexity condition [79]. If we present the strain energy function by an ANN, fulfilling all these conditions affects the ANN's architecture, which we explain in more detail in Sec. 3.2. Inserting Eq. (11) in Eq. (1) yields

$$\mathbf{S}^e = -p\mathbf{C}^{-1} + \sum_{r=1}^{R} \underbrace{2\left(\frac{\partial \Psi}{\partial \tilde{I}_r}\tilde{\mathbf{L}}_r - \frac{\partial \Psi}{\partial \tilde{J}_r}\mathbf{C}^{-1}\tilde{\mathbf{L}}_r\mathbf{C}^{-1}\right)}_{=\mathbf{S}_r^e} = -p\mathbf{C}^{-1} + \sum_{r=1}^{R} \mathbf{S}_r^e. \tag{12}$$

Nowadays, engineers can choose from a vast catalog of strain energy functions to model materials. Choosing a suitable strain energy function, however, typically requires expert knowledge. To overcome this problem, CANNs introduced a particularly efficient machine learning architecture to learn the relation between the argument in Eq. (11) and the resulting strain energy Ψ. Basing CANNs on Eq. (11) endows them with substantial prior knowledge from materials theory, namely, the theory of generalized invariants. This prior knowledge significantly reduces the amount of training data CANNs need to learn the constitutive behavior of a specific material of interest. At the same time, given the generality of the theory of generalized invariants, using Eq. (11) as a basis does not limit the generality of CANNs in any practically relevant way. Rather, the underlying neural network equips the constitutive model with the flexibility to adjust to experimental data from various materials without human guidance. In particular, the preferred material directions $\boldsymbol{l}_j$ and the scalar weight factors w_{rj} in Eq. (2) and Eq. (7) are learned by the CANN from the available material data. In the following, we extend this concept to anisotropic nonlinear viscoelasticity.

Remark. Our method relies on generalized structural tensors and their invariants. In principle, the classical structural tensors and their associated invariants, as outlined in tensors Eq. (2) and Eq. ((3), could be used. However, generalized structural tensors can be understood as an average measure of the anisotropy of a material. This averaging can significantly reduce the number of arguments required for functions like the strain energy function to describe the behavior of a specific material. Therefore, the generalized structural tensors and their corresponding invariants allow particularly lean information processing in neural networks and thus form the preferred basis for vCANNs.

2.2. Viscoelasticity

According to Fung [18], in QLV, the viscoelastic 2nd Piola–Kirchhoff stress tensor at current time t is given by the hereditary integral

$$\mathbf{S}(t) = \int_{-\infty}^{t} \mathbb{G}(t-s) : \dot{\mathbf{S}}^e \, \mathrm{d}s, \tag{13}$$

where $\mathbb{G}(t)$ is the time-dependent fourth-order reduced relaxation function tensor. $\dot{\mathbf{S}}^e$ is the material time derivative of the instantaneous elastic 2nd Piola–Kirchhoff stress tensor, i.e., $\dot{\mathbf{S}}^e = \frac{\mathrm{d}\mathbf{S}^e}{\mathrm{d}t}$, where $\mathbf{S}^e$ is computed according to Eq. (12).

The fundamental assumption of QLV is that $\mathbb{G}(t)$ depends only on time but not on the deformation (time-deformation separability) such that the relaxation behavior is the same for any applied deformation. To overcome this limitation, we allow $\mathbb{G}$ to depend on the deformation $\mathbf{C}$. At this point, we go beyond the framework of classical QLV because $\mathbb{G}$ is not only time-dependent anymore. We add the deformation rate $\dot{\mathbf{C}}$ to the arguments of $\mathbb{G}$ since many materials show not only strain-dependent but also strain rate-dependent viscoelastic behavior [2,80]:

$$\mathbf{S}(t) = \int_{-\infty}^{t} \mathbb{G}(t-s, \mathbf{C}, \dot{\mathbf{C}}) : \dot{\mathbf{S}}^e \, \mathrm{d}s. \tag{14}$$

In the simplest case, $\mathbb{G}(t) = G(t)\mathbb{I}$ where $G(t)$ denotes a scalar reduced relaxation function and $\mathbb{I}$ the fourth-order identity tensor. However, anisotropic materials may exhibit different viscous properties in different directions. Therefore, a single scalar reduced relaxation function would, in general, be insufficient to capture the complex nature of anisotropic viscoelastic materials. On the other hand, the experimental identification of a fourth-order reduced relaxation function tensor is highly challenging, even for simple classes of anisotropy, and is practically often unfeasible for complex classes. A reasonable compromise between practicability and generality of the constitutive model is to use a scalar-valued reduced relaxation function G_r for each stress contribution $\mathbf{S}_r^e$ in Eq. (12). Additionally, we augment the arguments of the reduced relaxation function with the structural tensors to account for anisotropy:

$$\mathbf{S}(t) = -p\mathbf{C}^{-1} + \sum_{r=1}^{R} \int_{-\infty}^{t} G_r(t-s, \mathbf{C}, \dot{\mathbf{C}}, \mathbf{L}_1, \mathbf{L}_2, \dots, \mathbf{L}_J) \, \dot{\mathbf{S}}_r^e \, \mathrm{d}s. \tag{15}$$

Experiments suggest that in many rubber materials and soft biological tissues, the viscous effects mostly attribute to the isochoric part of the stress [81]. In the incompressible limit, this holds exactly [82]. Therefore, in Eq. (15), the reduced relaxation functions G_r affect only the isochoric part of the stress.

The reduced relaxation functions G_r are scalar-valued functions of tensors. To fulfill the principle of material objectivity and to reflect the material symmetry correctly, the reduced relaxation functions have to be isotropic functions of the tensor system $\{\mathbf{C}, \dot{\mathbf{C}}, \mathbf{L}_1, \mathbf{L}_2, \dots, \mathbf{L}_J\}$ [76]. Compared to Eqs. (3) and (4), the set of isotropic invariants, in terms of which all other isotropic functions can be expressed, is completed by [77,78],

$$\operatorname{tr}\dot{\mathbf{C}}, \quad \operatorname{tr}\dot{\mathbf{C}}^2, \quad \operatorname{tr}\dot{\mathbf{C}}^3, \quad \operatorname{tr}\left(\dot{\mathbf{C}}\mathbf{L}_j\right), \quad \operatorname{tr}\left(\dot{\mathbf{C}}^2\mathbf{L}_j\right), \quad j = 1, 2, \dots, J, \tag{16}$$

$$\operatorname{tr}\left(\dot{\mathbf{C}}\mathbf{L}_i\mathbf{L}_j\right), \quad \operatorname{tr}\left(\mathbf{L}_i\mathbf{L}_j\right), \quad \operatorname{tr}\left(\mathbf{L}_i\mathbf{L}_j\mathbf{L}_k\right), \quad 1 \le i < j < k \le J, \tag{17}$$

$$\operatorname{tr}\left(\mathbf{C}\dot{\mathbf{C}}\right), \quad \operatorname{tr}\left(\mathbf{C}^2\dot{\mathbf{C}}\right), \quad \operatorname{tr}\left(\mathbf{C}\dot{\mathbf{C}}^2\right), \quad \operatorname{tr}\left(\mathbf{C}^2\dot{\mathbf{C}}^2\right), \quad \operatorname{tr}\left(\mathbf{C}\dot{\mathbf{C}}\mathbf{L}_j\right), \quad j = 1, 2, \dots, J. \tag{18}$$

Following the same arguments as before, we omit the invariants in Eqs. (17) and (18) yielding

$$G_r = G_r\Big(t, \operatorname{tr}\mathbf{C}, \operatorname{tr}\mathbf{C}^2, \operatorname{tr}\mathbf{C}^3, \operatorname{tr}\left(\mathbf{C}\mathbf{L}_1\right), \operatorname{tr}\left(\mathbf{C}^2\mathbf{L}_1\right), \dots, \operatorname{tr}\left(\mathbf{C}\mathbf{L}_J\right), \operatorname{tr}\left(\mathbf{C}^2\mathbf{L}_J,\right), \operatorname{tr}\dot{\mathbf{C}}, \operatorname{tr}\dot{\mathbf{C}}^2, \operatorname{tr}\dot{\mathbf{C}}^3, \dots, \operatorname{tr}\left(\dot{\mathbf{C}}\mathbf{L}_1\right), \operatorname{tr}\left(\dot{\mathbf{C}}^2\mathbf{L}_1\right), \operatorname{tr}\left(\dot{\mathbf{C}}\mathbf{L}_J\right), \operatorname{tr}\left(\dot{\mathbf{C}}^2\mathbf{L}_J\right)\Big). \tag{19}$$

By introducing the $2R+1$ generalized invariants

$$\tilde{I}_r = \operatorname{tr}\left(\dot{\mathbf{C}}\tilde{\mathbf{L}}_r\right), \qquad \tilde{J}_r = \operatorname{tr}\left[(\det\dot{\mathbf{C}})\dot{\mathbf{C}}^{-\mathrm{T}}\tilde{\mathbf{L}}_r\right] = \operatorname{tr}\left[(\operatorname{cof}\dot{\mathbf{C}})\tilde{\mathbf{L}}_r\right], \qquad \mathrm{III}_{\dot{\mathbf{C}}} = \det\dot{\mathbf{C}}, \qquad r = 1, 2, \dots, R \tag{20}$$

and the short-hand notations

$$\tilde{\mathcal{I}} = \left\{\tilde{I}_1, \tilde{J}_1, \dots, \tilde{I}_R, \tilde{J}_R, \mathrm{III}_{\dot{\mathbf{C}}}\right\}, \qquad \mathcal{I} = \tilde{\mathcal{I}} \cup \tilde{\mathcal{I}}, \tag{21}$$

we can express Eq. (19) alternatively by

$$G_r = G_r(t, \mathcal{I}). \tag{22}$$

Finally, we augment the arguments of the reduced relaxation function with the above-introduced feature vector $\mathbf{f}$:

$$G_r = G_r(t, \mathcal{I}, \mathbf{f}). \tag{23}$$

From Eq. (15), we obtain the 2nd Piola–Kirchhoff stress tensor

$$\mathbf{S}(t) = -p\mathbf{C}^{-1} + \sum_{r=1}^{R} \int_{-\infty}^{t} G_r(t-s, \mathcal{I}, \mathbf{f}) \, \dot{\mathbf{S}}_r^e \, \mathrm{d}s. \tag{24}$$

Prony series Motivated by linear viscoelasticity and the generalized Maxwell model (Fig. 1), the most popular choice for the reduced relaxation function G in QLV is the discrete Prony series

$$G(t) = g_\infty + \sum_{\alpha=1}^{N} g_\alpha \exp\left(-\frac{t}{\tau_\alpha}\right) \tag{25}$$

with

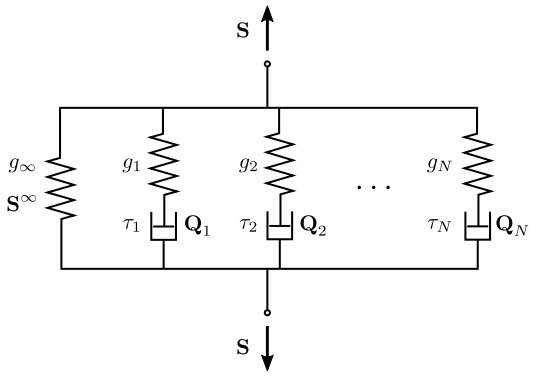

Fig. 1. The generalized Maxwell model: the elastic spring on the left represents the equilibrium stress response $\mathbf{S}^\infty$; each Maxwell element produces a viscous overstress $\mathbf{Q}_\alpha$ and represents a relaxation process with a different relaxation time. g_∞, g_i, and τ_i are constant material parameters or deformation (rate)-dependent functions.

$$g_\infty + \sum_{\alpha=1}^{N} g_\alpha = 1, \qquad 0 \leq g_\infty, g_\alpha \leq 1, \qquad \tau_\alpha > 0. \tag{26}$$

Here, g_∞ is a material parameter related to the equilibrium elasticity of the generalized Maxwell model, and g_α and τ_α are parameters characterizing elasticity and viscous relaxation time of the α-th Maxwell element. The g_∞ and g_α are referred to as relaxation coefficients. In principle, the number of Maxwell elements N is arbitrary, which enables the model to describe complex viscoelastic materials. Since the material parameters g_∞, g_α, and τ_α are constants, the classical Prony series is limited to linear viscoelasticity.

Generalized Prony series The classical Prony series does not depend on the deformation or the deformation rate but on time only. Therefore, to account for nonlinear viscoelasticity, we propose the following generalized Prony series

$$G_r = G_r(t, \mathcal{I}, \mathbf{f}) = g_{r\infty}(\mathcal{I}, \mathbf{f}) + \sum_{\alpha=1}^{N_r} g_{r\alpha}(\mathcal{I}, \mathbf{f}) \exp\left(-\frac{t}{\tau_{r\alpha}(\mathcal{I}, \mathbf{f})}\right), \qquad r = 1, 2, \dots, R. \tag{27}$$

The conditions Eq. (26) individually apply to the relaxation coefficients $g_{r\infty}(\mathcal{I}, \mathbf{f})$, $g_{r\alpha}(\mathcal{I}, \mathbf{f})$ and the relaxation times $\tau_{r\alpha}(\mathcal{I}, \mathbf{f})$ associated with the instantaneous elastic stress component $\mathbf{S}_r^e$. N_r denotes the number of Maxwell branches of the generalized Maxwell model associated with the instantaneous elastic stress component $\mathbf{S}_r^e$. In contrast to the classical Prony series, the relaxation coefficients and times in Eq. (25) are functions of the invariants $\mathcal{I}$ and the feature vector $\mathbf{f}$ to capture also anisotropic nonlinear viscoelasticity.

Inserting Eq. (27) into Eq. (24) yields

$$\mathbf{S}(t) = -p\mathbf{C}^{-1} + \sum_{r=1}^{R} \left[\mathbf{S}_r^\infty + \sum_{\alpha=1}^{N_r} \underbrace{\int_{-\infty}^{t} g_{r\alpha}(\mathcal{I}, \mathbf{f}) \exp\left(-\frac{t-s}{\tau_{r\alpha}(\mathcal{I}, \mathbf{f})}\right) \dot{\mathbf{S}}_r^e \, \mathrm{d}s}_{=\mathbf{Q}_{r\alpha}} \right] \tag{28}$$

$$= -p\mathbf{C}^{-1} + \sum_{r=1}^{R} \left[\mathbf{S}_r^\infty + \sum_{\alpha=1}^{N_r} \mathbf{Q}_{r\alpha} \right] \tag{29}$$

where $\mathbf{S}_r^\infty = g_{r\infty}(\mathcal{I}, \mathbf{f}) \mathbf{S}_r^e$ denotes the equilibrium stress associated with the r-th generalized Maxwell model. $\mathbf{Q}_{r\alpha}$ is the viscous overstress in the α-th Maxwell branch of the r-th generalized Maxwell model. To illustrate the proposed constitutive model, we particularized a vCANN for the important case of transverse isotropy in Appendix A. In general, closed-form solutions do not exist for the integrals in Eq. (28) so that a numerical time integration scheme has to be applied. Details are provided in Appendix B.

3. Machine learning architecture

3.1. General

In the previous section, we outlined the theoretical foundations of the model of nonlinear viscoelasticity on which we rely in this paper. The main idea of vCANNs is to implement this theory via a machine learning architecture. This architecture is illustrated in Fig. 2. In our approach, we use feedforward neural networks (FFNNs). The networks consist of L hidden layers. The input passed to the first layer is a vector $\boldsymbol{x}_0 \in \mathbb{R}^{n_0}$. The output of the l-th layer is denoted by $\boldsymbol{x}_l \in \mathbb{R}^{n_l}$, respectively, and computed as

$$\boldsymbol{x}_l = \sigma_l\left(\boldsymbol{x}_{l-1} \boldsymbol{W}_l + \boldsymbol{b}_l\right), \quad l = 1, \dots, L, \quad \boldsymbol{x}_l \in \mathbb{R}^{n_l}, \tag{30}$$

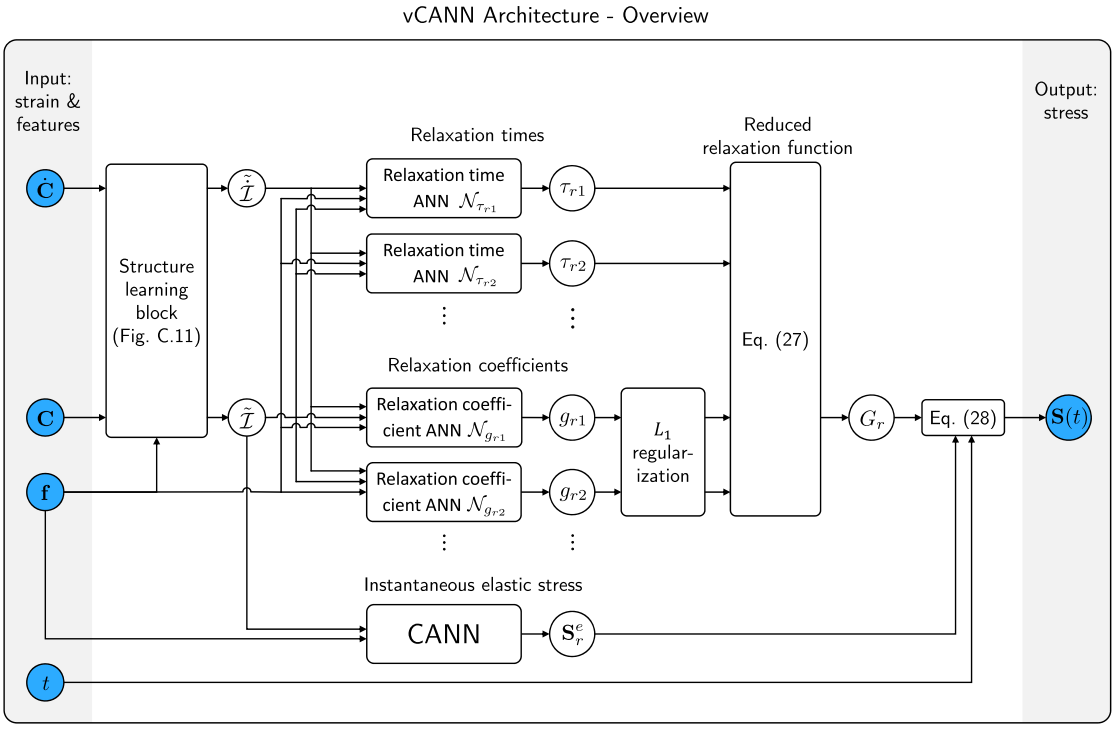

Fig. 2. Schematic illustration of the vCANN architecture: The strain (rate) tensors $\mathbf{C}$, $\dot{\mathbf{C}}$, and the feature vector $\mathbf{f}$ serve as input to the structure learning block (Fig. C.1) which learns the generalized invariants $\tilde{I}$ and $\tilde{\mathcal{I}}$. The generalized invariants and the feature vector are fed to the relaxation time ANNs $\mathcal{N}_{\tau_{r\alpha}}$ and relaxation coefficient ANNs $\mathcal{N}_{g_{r\alpha}}$. The outputs of $\mathcal{N}_{\tau_{r\alpha}}$ are the relaxation times $\tau_{r\alpha}$. The neural networks $\mathcal{N}_{g_{r\alpha}}$ calculate the relaxation coefficients $g_{r\alpha}$ which are regularized to promote a sparse model (grey box 'L_1 regularization'). The reduced relaxation function G_r is obtained by inserting $\tau_{r\alpha}$ and $g_{r\alpha}$ in Eq. (27). The generalized invariants $\tilde{I}$ and $\mathbf{f}$ are fed to the CANN which calculates the instantaneous elastic stress contributions $\mathbf{S}_r^e$. The internal structure of the CANN is depicted in Fig. 1(a) in [72]. With the current time t as an additional input, we finally calculate the viscoelastic stress $\mathbf{S}(t)$ at time t using Eq. (28). Note that Fig. C.1 is slightly modified compared to Fig. 1(b) in [72] since vCANNs use $\dot{\mathbf{C}}$ as an input, too.

with the activation function $\sigma_l(\cdot)$ of layer l, weights $\boldsymbol{W}_l \in \mathbb{R}^{n_{l-1} \times n_l}$ of layer l, and biases $\boldsymbol{b}_l \in \mathbb{R}^{n_l}$ of layer l. The activation function is applied element-wise to its argument. The output of the last layer (and thus the output of the network altogether) is $\boldsymbol{x}_L \in \mathbb{R}^{n_L}$. Mathematically, an FFNN with L hidden layers establishes a mapping $\mathcal{N} : \mathbb{R}^{n_0} \to \mathbb{R}^{n_L}$, $\boldsymbol{x}_L = \mathcal{N}(\boldsymbol{x}_0)$.

Applying the model of nonlinear viscoelasticity outlined in Sec. 2 to compute the stress at each point in time (depending on the strain history) requires implementing Eq. (15). To evaluate this equation for a given strain history, we have to define the following functions: the strain energy Ψ and the reduced relaxation functions G_r.

3.2. Strain energy

To define the strain energy, we use a CANN [72] relying on the generalized invariants of the type $\tilde{I}$. Stresses can be computed by automatic differentiation. The CANN automatically ensures material objectivity, material symmetry, and an energy- and stress-free reference configuration, i.e., $\Psi(\mathbf{C} = \mathbf{I}) = 0$ and $\mathbf{S}(\mathbf{C} = \mathbf{I}) = \mathbf{0}$. The latter is ensured by a term in the strain energy that is continuously adapted during the training procedure such that these two conditions remain satisfied. Non-negativeness of the strain energy function, i.e., $\Psi \geq 0$, is ensured by choosing appropriate activation functions and weight constraints in the last two layers of the CANN. In the second-to-last layer, we apply non-negative activation functions $\sigma_L : \mathbb{R} \to \mathbb{R}^{+0}$. In the last layer, we apply a linear activation function $\sigma_L(\boldsymbol{x}) = \boldsymbol{x}$ and enforce non-negative weights and biases ($\boldsymbol{W}_L, \boldsymbol{b}_L \geq 0$), yielding a non-negative strain energy function. Except for the last layer, where we apply a linear activation function, our default activation function is the softplus function $\sigma_l(x) = \ln(1 + \exp(x))$. Apart from the useful property of being positive, the softplus function is a C^∞-continuous function. Hence, the strain energy function, stress tensor, and elasticity tensor are C^∞-continuous functions which is numerically favorable, particularly for implementing the vCANN in FE software.

Note that, if necessary, we can easily guarantee polyconvexity [79] of the strain energy function when using CANNs. To this end, we enforce non-negative weights in all layers and non-negative biases in the last layer (but not necessarily in the previous layers [83]). Then, applying convex, non-decreasing activation functions on all layers renders the network convex [84]. We meet this constraint on the activation functions by default since we use linear activation functions in the last layer and softplus activation functions in all other layers. Both activation functions are convex and non-decreasing. Using a neural network with the above features, we only have to ensure that only polyconvex invariants are used in the CANN. In particular, the generalized invariants of the type $\tilde{I}$ are polyconvex [73]. For an overview of other polyconvex invariants, the reader is referred to [85–87].

3.3. Reduced relaxation functions

To define the reduced relaxation functions G_r in Eq. (27), we must define strain (rate)-dependent relaxation times and relaxation coefficients. To this end, we represent the unknown relation between the strain (rate) and these parameters by FFNNs. We employ separate FFNNs for each relaxation time and coefficient such that each neural network can focus on a particularly simple task. The constraints on the reduced relaxation functions, (26), are less severe than those on the strain energy functions. The positivity of the relaxation times and coefficients in Eq. $(26)_{2,3}$ is guaranteed by the same methods described above for the strain energy function. The unity constraint on the relaxation coefficients, Eq. $(26)_1$, is enforced by a custom normalization layer. Apart from that, the functional relations providing the sought parameters are not restricted. Note that using the invariant basis $\mathcal{I}$ as input, the relaxation times and coefficients automatically ensure material objectivity and material symmetry.

The number of Maxwell elements in the generalized Prony series is an important parameter. With sufficiently many Maxwell elements, a Prony series can describe arbitrarily complex viscoelastic materials. Often, materials exhibit numerous different relaxation times [88]. A generalized Maxwell model represents each relaxation time by a different Maxwell element. Following these arguments, choosing a large number of Maxwell elements is preferable to represent the relaxation behavior as accurately as possible. However, the model complexity, and thus the computational cost, increases with the number of Maxwell elements. Moreover, complex models with many parameters tend to overfit the experimental data, thereby losing the ability to generalize beyond specific given training data. From that perspective, keeping the number of relaxation times and coefficients small is favorable. To balance between an accurate representation of data and a low model complexity, we proceed as follows.

Identifying the relaxation coefficients and times of a generalized Maxwell model is known to be an ill-posed problem [89]. Therefore, in classical approaches, the number of Maxwell elements N_r is determined beforehand and fixed during the parameter identification process [90]. In some approaches, the number of Maxwell elements and the relaxation times are determined a priori and fixed during parameter identification to remove ill-posedness [89]. In our approach, we predefine a maximum number of Maxwell elements N_r^{max}. During the training, the actual number N_r of Maxwell elements is determined by the vCANN as a part of the learning process within the allowed range $[1; N_r^{max}]$. To avoid unnecessary constraints to the learning process, one may choose relatively large values for N_r^{max}, which typically result after the training in $N_r \ll N_r^{max}$.

The literature shows that the relaxation processes of viscoelastic materials take place at different timescales [88]. These relaxation timescales are typically uniformly distributed on a logarithmic scale to model the viscoelastic material behavior [91]. To endow our machine learning architecture with this heuristic prior knowledge, we scaled the output of the N_r^{max} FFNNs that learned the relaxation times by time constants $T_{r\alpha}$, $\alpha = 1, 2, \dots, N_r^{max}$. These time constants were uniformly distributed on a logarithmic scale in the range $[T_{min}, T_{max}]$. A uniform spacing of the time scaling constants on the logarithmic scale within the interval $[T_{min}, T_{max}]$ ensures that all timescales are equally represented. T_{min} and T_{max} are parameters initially defined by the user based on prior knowledge or heuristic expectations. In practice, the experimental setup and available experimental equipment set the theoretical limits on the observable timescales. While the total length of an experiment determines the longest timescale T_{max}, the highest data sampling rate determines the shortest timescale T_{min}. However, depending on the objectives of a research project, one may choose other timescale limits than these theoretical limits. It is important to underline that the time scaling constants $T_{r\alpha}$ are not the relaxation times of our model. The vCANN can, and will in general, learn relaxation times $\tau_{r\alpha}$ (possibly even considerably) differing from the $T_{r\alpha}$. Yet, the time constants $T_{r\alpha}$ provide via the scaling of the output of the FFNNs some bias regarding the expected timescales for the different relaxation times, which can significantly accelerate the training if $[T_{min}, T_{max}]$ is properly chosen. In Appendix D, Fig. D.1, we illustrate the influence of different choices for T_{min} and T_{max}.

Initially, we prescribe the maximum number of Maxwell elements N_r^{max}, typically much larger than the actual number N_r required to accurately describe the viscoelastic material. This allows us to gradually eliminate Maxwell elements during training to obtain a sparse model. This approach is similar to the one of [92,93], where the number of Maxwell elements was adjusted by merging or removing them during parameter identification to avoid ill-posedness and improve the fit. Likewise, [94] proposed to apply Tikhonov-regularization [95] to the material parameters and subsequently cluster Maxwell elements with similar relaxation times. We decided to promote sparsity of our model by applying L_1 regularization to the relaxation coefficients $g_{r\alpha}$, $\alpha = 1, 2, \dots, N_r^{max}$. Using L_1 regularization, the optimal value for some relaxation coefficients will be zero, eliminating the corresponding Maxwell elements. In this approach, one uses a penalty, or sparsity, parameter Λ controlling the sparsity of the model. Choosing $\Lambda = 0$ disables regularization, whereas with increasing Λ, the sparsity of the model increases, too. Being a hyperparameter, the sparsity parameter Λ has to be predefined and possibly iteratively optimized. To this end, starting from $\Lambda = 0$, one trains the vCANN with increasing values of Λ and monitors the loss and the number of active Maxwell elements. Following the law of parsimony, the optimal value of Λ results in a vCANN that balances the model's validation loss and parsimony. To illustrate the influence of Λ, we trained the same vCANN for different values of Λ. In Appendix E, Fig. E.1, we provide the corresponding loss curves and the number of active Maxwell elements as a function of the training epochs.

In summary, relaxation times and coefficients, as functions of the invariants $\mathcal{I}$ and the feature vector $\mathbf{f}$, are learned by individual FFNNs. Scaling of the FFNNs determining the relaxation times by predefined logarithmically uniformly spaced constants introduces a bias in agreement with the literature findings that can help accelerate the training process. L_1 regularization on the relaxation coefficients promotes sparse reduced relaxation functions. We implemented the complete vCANN framework using Keras [96], the high-level API of the open-source machine learning platform TensorFlow [97].

4. Results

In this section, we apply vCANNs to various data sets. We use synthetic as well as experimental data. In [72], we already demonstrated that CANNs could successfully learn the preferred material directions $\boldsymbol{I}_{rj}$ and the scalar weight factors w_{rj} in Eq. (2). Therefore, for simplicity, we herein assume them to be known to focus on this paper's main problem, nonlinear viscoelasticity. We list the corresponding vCANNs and their hyperparameters in Appendix I for each of the following examples. There, we also provide additional information on the training procedure.

4.1. Anisotropic viscoelasticity with synthetic data

We created synthetic training data to mimic stress-strain data of viscoelastic soft biological tissues. To this end, we used two hyperelastic constitutive models popular in biomechanics, the Ogden model [98], and the Holzapfel–Gasser–Ogden (HGO) model [99]. The Ogden model is a phenomenological model for isotropic rubber-like materials and soft biological tissues and is usually formulated in terms of the principal stretches λ_i, $i = 1,2,3$, which are the square roots of the eigenvalues of $\mathbf{C}$,

$$\Psi_{\mathrm{OG}}(\mathbf{C}) = \sum_{p=1}^{n} \frac{\mu_p}{\alpha_p} \left(\lambda_1^{\alpha_p} + \lambda_2^{\alpha_p} + \lambda_3^{\alpha_p} - 3 \right). \tag{31}$$

In Eq. (31), n is a positive integer, μ_p and α_p are (constant) material parameters. Many soft biological tissues exhibit stiffening fibers that induce anisotropy. Therefore, the Ogden model is often combined with the HGO model, which adds an anisotropic contribution to the total strain energy function. The strain energy function of the HGO model, with one preferred material direction $\boldsymbol{l}$ and structural tensor $\mathbf{L} = \boldsymbol{l} \otimes \boldsymbol{l}$, is

$$\Psi_{\mathrm{HGO}}(\mathbf{C},\mathbf{L}) = \begin{cases} \frac{k_1}{2k_2} \left\{ \exp\left[k_2 (I_4 - 1)^2\right] - 1 \right\} & \text{for } I_4 \geq 1, \\ 0 & \text{for } I_4 < 1. \end{cases} \tag{32}$$

$k_1 > 0$ and $k_2 > 0$ are material parameters, and $I_4 = \mathbf{C} : \mathbf{L}$. Since I_4 represents the squared fiber stretch, $I_4 < 1$ means compression of the fibers, which are assumed to bear load under tension only. Thus, for $I_4 < 1$, the anisotropic strain energy and stress contributions are assumed to be zero.

To produce synthetic data, we used a material model where the total strain energy was a sum of the Ogden (OG) and HGO strain energy functions, that is,

$$\Psi = \Psi_{\mathrm{OG}} + \Psi_{\mathrm{HGO}}. \tag{33}$$

For the viscous part of the constitutive model used for generating synthetic material data, we assumed strain-dependent relaxation times and coefficients:

$$\tau_i^{\mathrm{OG}}(I_1) = \hat{\tau}_{a,i}^{\mathrm{OG}} \exp\left(\hat{\tau}_{b,i}^{\mathrm{OG}} (I_1 - 3)^2 \right), \qquad g_i^{\mathrm{OG}}(\lambda) = \hat{g}_{a,i}^{\mathrm{OG}} \exp\left(\hat{g}_{b,i}^{\mathrm{OG}} (I_1 - 3)^2 \right), \qquad i = 1,2 \tag{34}$$

$$\tau_1^{\mathrm{HGO}}(I_4) = \hat{\tau}_a^{\mathrm{HGO}} \exp\left(\hat{\tau}_b^{\mathrm{HGO}} (I_4 - 1)^2 \right), \qquad g_1^{\mathrm{HGO}}(I_4) = \hat{g}_a^{\mathrm{HGO}} \exp(\hat{g}_b^{\mathrm{HGO}} (I_4 - 1)^2), \tag{35}$$

where, $\hat{\tau}_{a,i}^{\mathrm{OG}}$, $\hat{\tau}_{b,i}^{\mathrm{OG}}$, $\hat{g}_{a,i}^{\mathrm{OG}}$, $\hat{g}_{b,i}^{\mathrm{OG}}$, $\hat{\tau}_a^{\mathrm{HGO}}$, $\hat{\tau}_b^{\mathrm{HGO}}$, $\hat{g}_a^{\mathrm{HGO}}$, and $\hat{g}_b^{\mathrm{HGO}}$ are material parameters. The superscripts $(\cdot)^{\mathrm{OG}}$ and $(\cdot)^{\mathrm{HGO}}$ indicate whether the relaxation times and coefficients correspond to the reduced relaxation function of the isotropic part Ψ_{OG} or the anisotropic part Ψ_{HGO}. Using the material parameter values in Table F.1 and Table F.2 for Eqs. (34) and (35), we simulated uniaxial cyclic tension-compression experiments with relaxation periods between each tension and compression period. After each complete cycle the stretch rate $\dot{\lambda}$ was changed according to the sequence $\dot{\lambda} = (0.02 \to 0.03 \to 0.04 \to 0.05)\ \mathrm{s}^{-1}$. Loading and unloading periods took $t_{move} = 10$ s, respectively. The relaxation periods took $t_{relax} = 60$ s. Thus, a single cycle took $t_{cyc} = 160$ s and the total experiment $t_{total} = 640$ s. Synthetic training data were generated for different preferred directions, characterized by the acute angle φ between the loading and preferred material directions. $\varphi = 0°$ means that loading direction and preferred direction $\boldsymbol{l}$ are parallel, $\varphi = 90°$ means that both are orthogonal. The synthetic training data comprised stress data from fictitious materials with four different preferred directions corresponding to $\varphi \in \{0, 15, 20, 25\}$ °.

To validate the model, we generated additional synthetic data for a material with the preferred direction $\varphi = 10°$, which is not in the training data set. For this material, we simulated two more loading cycles in addition to the above-described loading history, such that the vCANN had to extrapolate the stress response temporally. The stretch rate of the cycles changed according to the sequence $\dot{\lambda} = (0.01 \to 0.02 \to 0.03 \to 0.04 \to 0.02 \to 0.05)\ \mathrm{s}^{-1}$.

We trained a vCANN with the transversely isotropic structure and hyperparameters given in Appendix I.1, Table I.1. Figures 3 and 4 show that the vCANN learns to replicate the training data almost exactly. In compression, the stress response is similar for all preferred directions since only the isotropic matrix of the composite (Ogden model) bears the load. The vCANN replicates this feature accurately. Similarly, the prediction of the validation data set for the unknown preferred direction captures and extrapolates almost perfectly the material response. In particular, the irregular stress response in the time interval [640, 710] s, caused by halving the stretch rate, is predicted precisely.

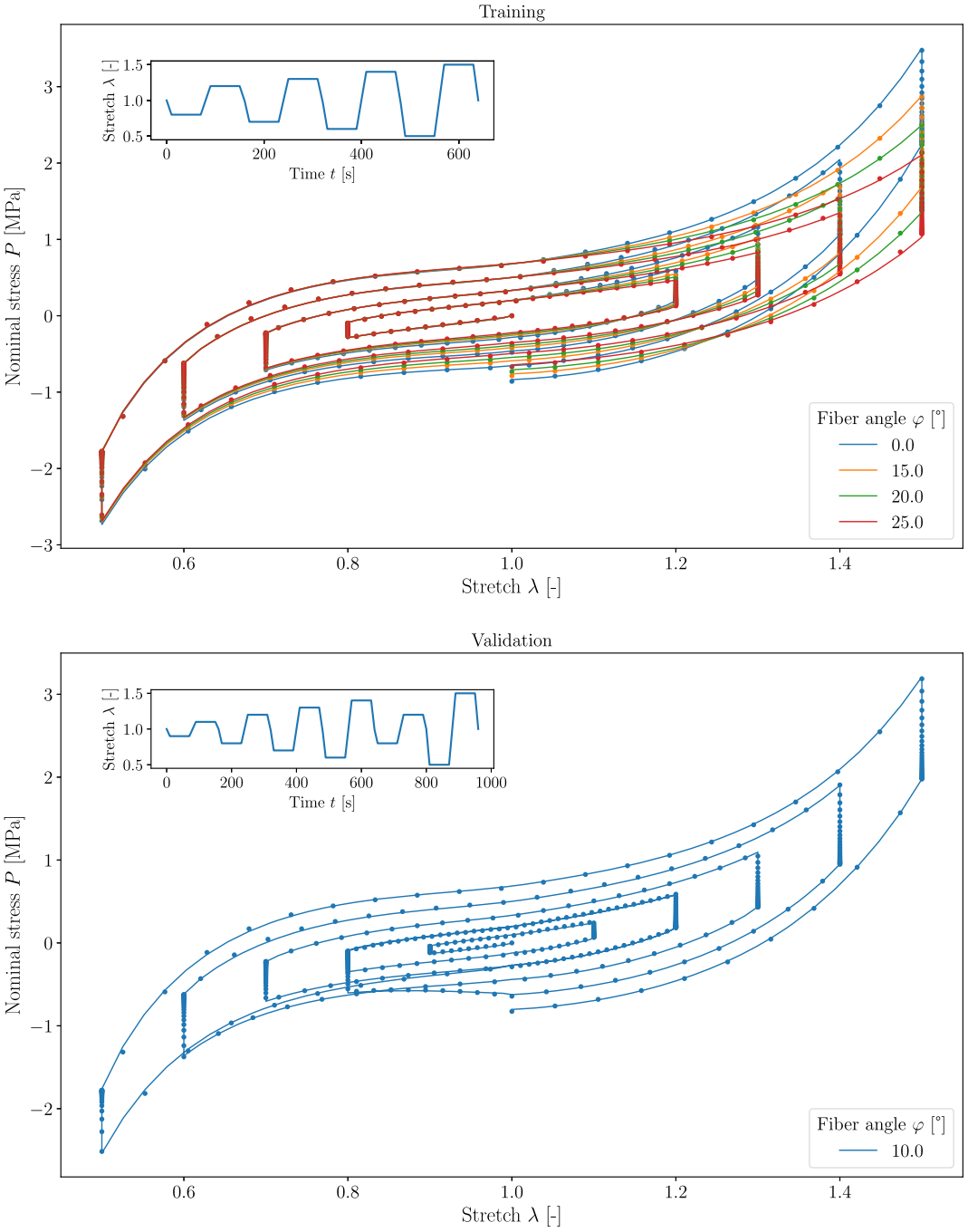

Fig. 3. Training (top) and validation (bottom) results. The dotted lines represent the synthetic training and validation data; the solid lines represent the vCANN predictions. (For interpretation of the colors in the figure(s), the reader is referred to the web version of this article.)

4.2. Passive viscoelastic response of the abdominal muscle

We reproduced relaxation responses of the leporine rectus abdominis muscle reported in [37]. The reduced relaxation function's shape depends on the stretch level, thus exhibiting nonlinear viscoelastic behavior. Classical QLV cannot account for this stretch dependence and would predict the same curve for each stretch level. To represent the stretch-dependent relaxation behavior, [37] incorporated stretch-dependent relaxation coefficients and times into a Prony series with one Maxwell element. The authors empirically determined the phenomenological strain dependence of the relaxation coefficients and times. However, their model did not accurately capture the reduced relaxation curves despite utilizing optimization algorithms to fit the material parameters to ex-

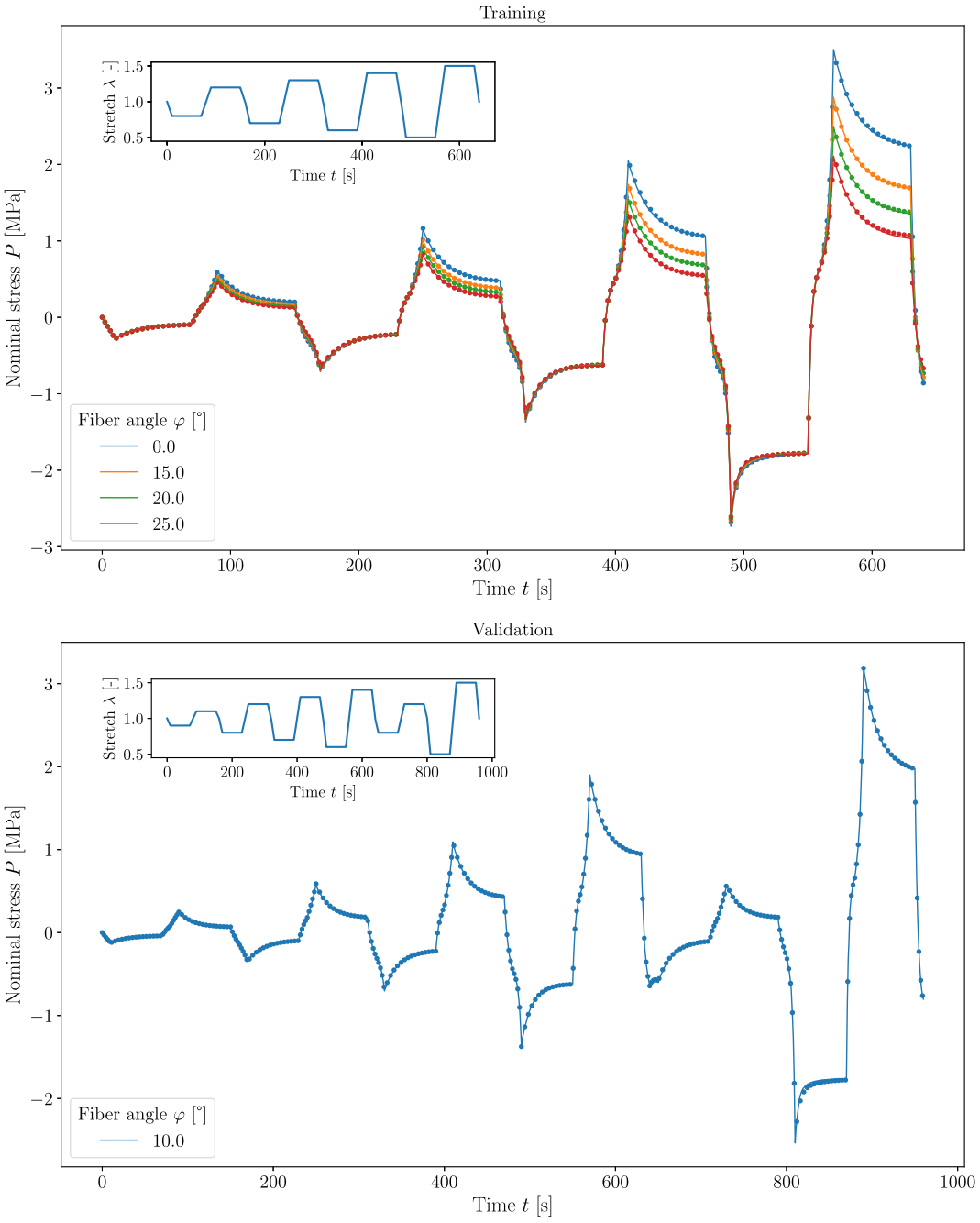

Fig. 4. Training (top) and validation (bottom) results. The dotted lines represent the synthetic training and validation data; the solid lines represent the vCANN predictions.

perimental data (cf. Fig. 10 in [37]). This illustrates the limits of human-designed and human-calibrated constitutive models for viscoelastic materials.

In contrast, the vCANN captures the relaxation curves with high accuracy (Fig. 5) otherwise only matched by much more complex FNLV models based on the multiplicative split of the deformation gradient, see Fig. 5 in [53] (reproduced in Appendix G.2, Fig. G.1) for comparison on the same experimental data set. We trained the vCANN with only four relaxation curves and withheld two for validation. The FNLV model, however, was fitted to all six relaxation curves. Yet the vCANN precisely represents all relaxation curves, especially their initial rapid decay. We initialized the vCANN with $N_{max} = 10$ Maxwell elements. Six of them were discarded during training, leaving only the reduced set of parameters plotted in Fig. 6. We provide the trained vCANN structure and the corresponding hyperparameters in Appendix I.2, Table I.2.

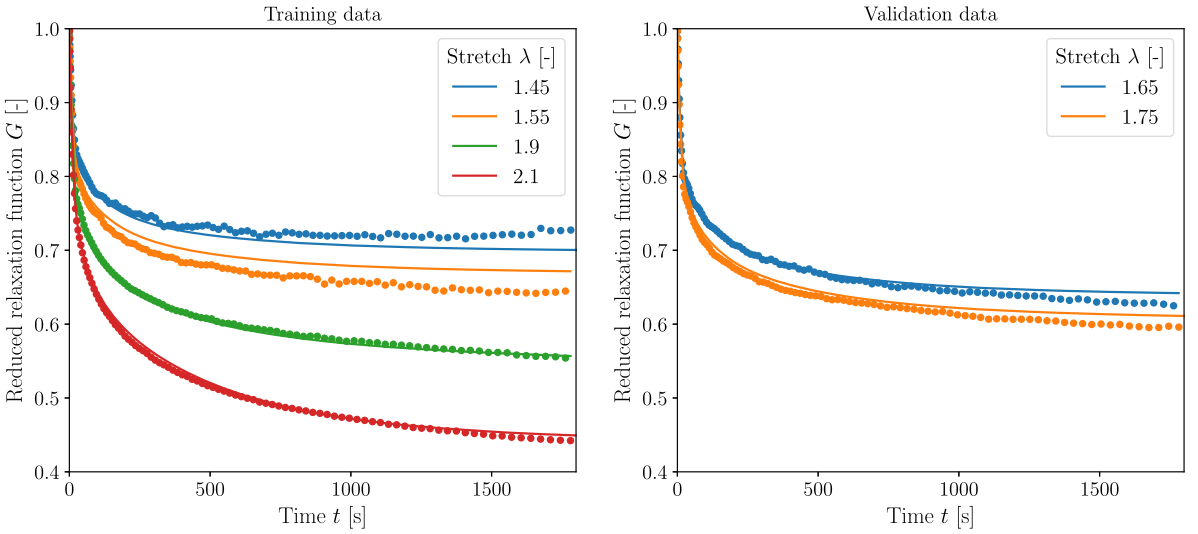

Fig. 5. vCANNs can learn to replicate (left) and predict (right) the viscoelastic behavior of abdominal muscle with high accuracy: experimental data from Fig. 4(b) of [37] is represented by dotted lines; the solid lines represent the achieved fitting of the vCANN on the training data (left) and the predictive performance on the validation data (right).

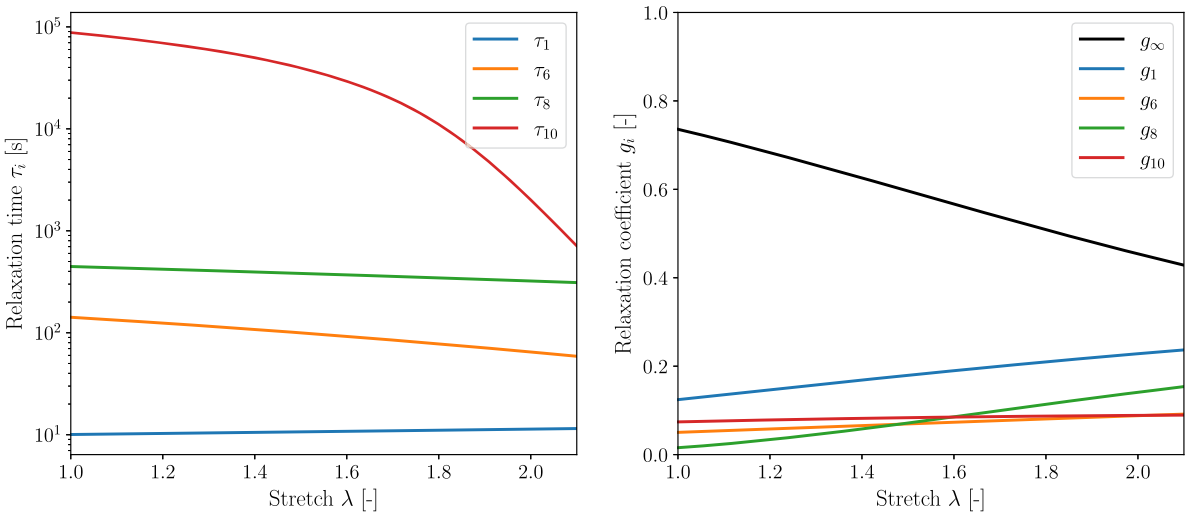

Fig. 6. Relaxation times (left) and coefficients (right) learned by the vCANN from the data set of leporine rectus abdominis muscle by [37]. Only four of the initial ten Maxwell elements remained after training.

4.3. Viscoelastic modeling of VHB 4910

Very-High-Bond (VHB) 4910 is a soft electro-active polymer (EAP) that exhibits nonlinear viscoelastic behavior and can undergo substantial deformations. VHB 4910 was experimentally studied by [100], using uniaxial loading-unloading tests to characterize the rate-dependent behavior. The tests were conducted for three different stretch rates $\dot{\lambda} \in \{0.01, 0.03, 0.05\}$ s^{-1} and four different stretch levels $\lambda \in \{1.5, 2.0, 2.5, 3.0\}$ (Fig. J.1). Moreover, the authors conducted a multi-step relaxation test to determine the equilibrium response of the material. The constitutive model proposed in [100] is based on a multiplicative split of the deformation gradient into an elastic and viscous part. The hyperelastic eight-chain model of [101] was chosen to model the elastic part. The material parameters of the elastic part were identified using the data from a multi-step relaxation test. The strain energy function and evolution equation proposed by [102] were chosen for the viscous part. Their viscous material parameters were identified using the loading-unloading data of $\dot{\lambda} = 0.01$ s^{-1} and $\dot{\lambda} = 0.05$ s^{-1} at a stretch level of $\lambda = 3$, Fig. 7(a). The rheological analog model of the constitutive model was a generalized Maxwell model where the number of parallel branches was determined by hand to be four.

A few years later, the same experimental data of VHB 4910 were again studied to demonstrate the abilities of a novel advanced microstructurally-informed constitutive model developed in [103]. The model relies on advanced knowledge of continuum and statistical mechanics and uses a multiplicative decomposition of the deformation gradient to represent a generalized Maxwell behavior. The elastic material parameters of the model were identified using time-consuming quasi-static tensile tests. The viscous material

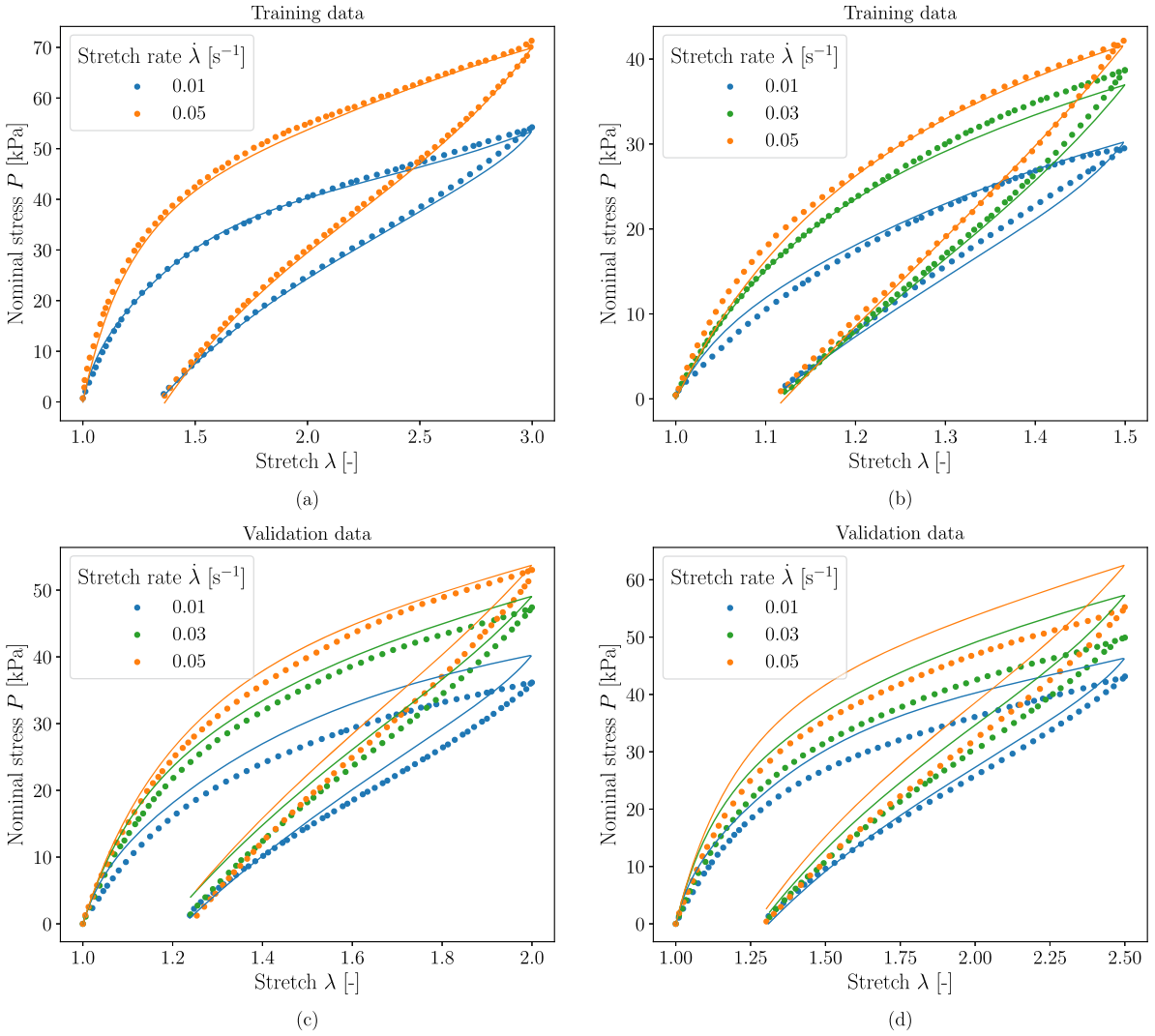

Fig. 7. Results of the trained vCANN for the polymer VHB 4910: achieved fitting of training data (a)–(b) and predictive performance on the validation data (c)–(d). Each subfigure shows the loading-unloading stress response for a fixed maximum stretch but different stretch rates. The dotted lines represent experimental data of VHB 4910 reproduced from [100]; the solid lines represent the trained vCANN.

parameters were identified using all loading-unloading experiments depicted in Figs. 7(a)–(c), excluding, however, data with a maximum stretch of $\lambda = 2.5$, Fig. 7(d). The number of Maxwell elements was determined by hand and set to three.

By contrast, we only used loading-unloading data with $\dot{\lambda} = 0.01$ s^{-1} and $\dot{\lambda} = 0.05$ s^{-1} at the stretch levels $\lambda = 1.5$ and $\lambda = 3$ to train the vCANN. Figure 7 shows the training and validation results. The fit of both the training and validation is very accurate and at least on par with the fits of the FNLV models proposed in [100] (reproduced in Appendix G.2, Figs. G.2 and G.3), and [103] (reproduced in Appendix G.2, Figs. G.5 and G.4). However, we note that the vCANN automatically learned the number of Maxwell elements required to represent the material behavior well. We initialized the vCANN with 10 Maxwell elements. After training, only two remained the viscous properties of which we provide in Fig. 8. Moreover, the application of the vCANN did not require advanced expert knowledge and did not require data from particularly sophisticated experiments. These advantages make vCANNs attractive from a practical point of view, in particular in the context of industrial applications. We list the details on the trained vCANN structure and the corresponding hyperparameters in Appendix I.3, Table I.3.

Remark. The relatively large differences between the experimental data and the vCANN model for $\lambda = 2.5$ in Fig. 7(d), which can also be observed for the FNLV model in [100], are likely a result of experimental scatter. The loading paths should be almost identical for a fixed strain rate up to the respective maximum stretches. However, this is not the case, as is highlighted in Fig. J.1, which suggests considerable measurement errors in a part of the data, which naturally limited the ability of the vCANN to derive a consistent data-driven model.

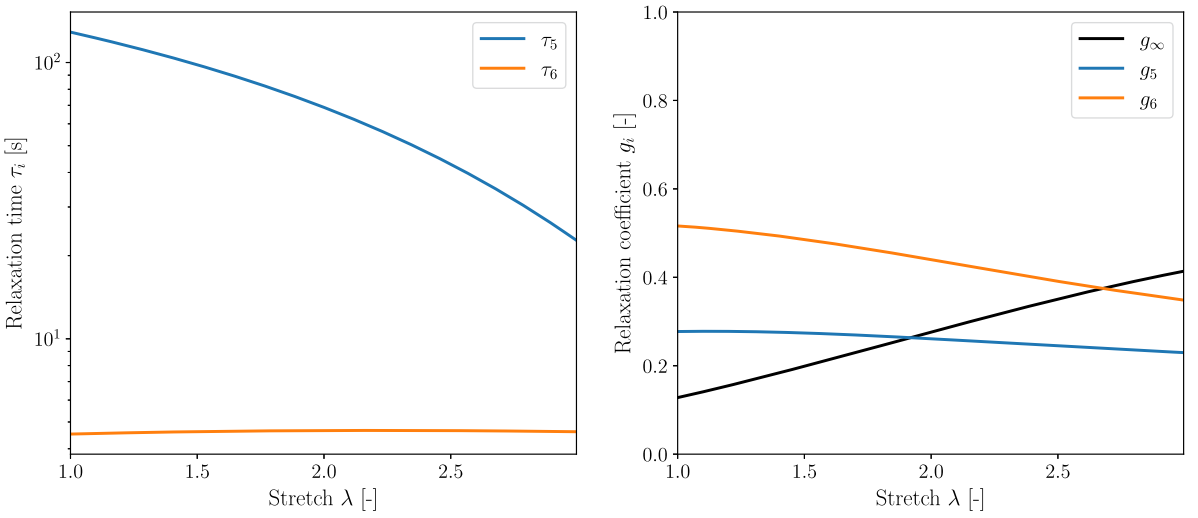

Fig. 8. Viscous properties of the vCANN learned from experimental data on VHB 4910 from [100]. Two of the initial 10 Maxwell elements were kept and are necessary to describe the material accurately.

4.4. *Blast load analysis of polyvinyl butyral*

Polyvinyl Butyral (PVB) is a polymer whose primary application is laminated safety glasses. Under heat and pressure, two glass panes are bonded with an interlayer of PVB into a single unit. Under blast loads, the interlayer binds shards of glass, absorbs energy, and mitigates its transfer to the surrounding frame. It is essential to understand the mechanical behavior of PVB to improve the design of laminated glass structures. Large-scale simulations of these structures require simple material models that capture the mechanical behavior over a wide range of strain rates. Del Linz et al. [104] conducted high-stretch rate experiments on PVB, with stretch rates between 0.01 s^{-1} and 400 s^{-1}. The viscous properties of PVB likely vary within such a wide range of strain rates. The significant change of the stress-stretch curve's shape above 0.2 s^{-1}, visible in Fig. 9, suggests this, too. Ideally, the constitutive model should be able to represent this transition accurately. The authors of [104] proposed an FNLV model and used the strain-dependent viscosity function by [47]. The model describes the experimental data well at high stretch rates, although it cannot accurately resolve the peak stress and subsequent softening at $\lambda \approx 1.2$. At low strain rates, the fit quality is quantitatively unsatisfactory. In [104], the authors also fitted a standard generalized Maxwell model with constant relaxation coefficients and times for comparison. The model comprised six Maxwell elements whose relaxation times were chosen to be uniformly distributed on the logarithmic scale and kept fixed during the parameter identification of the relaxation coefficients. Notably, to account for the broad stretch rate range, two

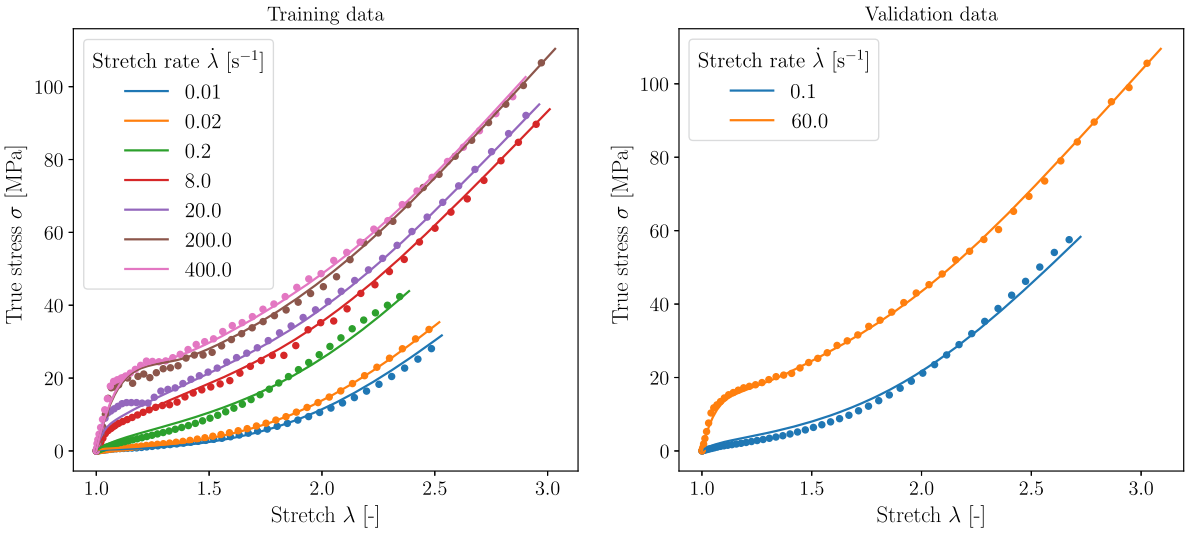

Fig. 9. High-stretch rate experiments on PVB. The vCANN accurately describes the constitutive behavior over a wide range of stretch rates for the training (left) and unknown validation data (right). The dotted lines represent experimental data reproduced from [105]; the solid lines represent the achieved fitting of the vCANN on the training data (left) and the predictive performance on the validation data (right).

different models had to be used, one for the low stretch rate regime (up to 8 s^{-1}) and the other for the high stretch rate regime (20 s^{-1} and above). However, neither model could accurately describe the material behavior in their respective stretch rate regimes. Unfortunately, neither for the FNLV model nor for the standard generalized Maxwell model, simulation results for the stretch rates $\dot{\lambda} = 0.1$ and 60 s^{-1} are reported in [104]. As delineated below, we used these strain rates to validate our vCANN.

We trained the vCANN detailed in Appendix I.4, Table I.4 to account for the rate-dependent viscoelastic behavior. Figure 9 shows that the vCANN successfully learned the constitutive behavior over a wide range of stretch rates. Comparing Figs. 12–17 in [104] (reproduced in Appendix G.3, Figs. G.6–G.8) with Fig. 9, reveals that the trained vCANN outperforms the traditional models. In particular, they capture the peak stress and softening in the initial loading phase up to $\lambda \approx 1.2$. Importantly, the data-driven nature of our approach apparently provided the flexibility to model the transition between the low and high stretch rate regimes. In contrast, two different classical models were required to capture the two different regimes. The vCANN did not only learn the constitutive behavior of the training data but also made precise predictions in the low and high stretch regimes for the unknown validation data. Remarkably, no advanced expert knowledge was necessary to apply the vCANN, and training the vCANN from scratch took less than 10 minutes on a standard desktop computer.

4.5. Thermo-viscoelastic modeling of VHB 4905

Another commercially available EAP is VHB 4905. Like most polymers, VHB 4905 is strongly temperature-sensitive. Hence [105] conducted an extensive experimental study with a wide range of temperatures at different stretch rates and stretch levels. To demonstrate the utility of the feature vector $\mathbf{f}$ in the vCANN architecture (which is optional and was not yet used in the previous examples), we included the temperature Θ into the vCANN input as $\mathbf{f}$. For training we used data of loading-unloading tests with different temperatures $\Theta \in \{0, 10, 20, 40, 60, 80\}$ °C and stretch rates $\dot{\lambda} \in \{0.03, 0.1\}$ s^{-1} at the stretch level $\lambda = 4$. Additionally, we included in the training set data of tests with $\Theta \in \{0, 40, 60, 80\}$ °C, $\dot{\lambda} = 0.1$ s^{-1} at $\lambda = 2$, Fig. 10. The strong nonlinear temperature dependence of the stress response is visible by comparing Fig. 10(a) and Fig. 10(c). In particular, the shape of the stress-stretch curve as well as the stiffness changes between 0 °C and 20 °C significantly.

To validate the trained vCANN, we took data from loading-unloading tests with $\Theta \in \{0, 10, 20, 40, 60, 80\}$ °C, $\dot{\lambda} = 0.03$ s^{-1} at $\lambda = 3$. Moreover, we used data from tests with $\Theta \in \{0, 10, 20, 40, 60, 80\}$ °C, $\dot{\lambda} = 0.05$ s^{-1} at $\lambda = 4$ for validation, Figs. 11. Of note, the vCANN had not received any training data with a stretch level $\lambda = 3$ nor with a stretch rate $\dot{\lambda} = 0.05$ s^{-1}. Yet, the trained vCANN was able to predict very well the material behavior for the unknown stretch level and also for the unknown stretch rate. Both is challenging for classical constitutive models and demonstrates the potential of vCANNs. In Appendix H, we have additionally assessed the vCANN's performance to extrapolate the thermo-viscoelasticity of VHB 4905 to temperature levels beyond the training regime. Details on the trained vCANN and its hyperparameters are documented in Appendix I.5, Table I.5. As seen in [105], different sophisticated load protocols are necessary for classical models to calibrate individual parts of the model separately. Although this procedure is possible with vCANNs due to their modularity, they can be trained on the entire data set directly, which is much simpler, faster, and requires no advanced expert knowledge.

5. Conclusion

In this paper, we introduced vCANNs, a physics-informed data-driven framework for anisotropic nonlinear viscoelasticity at finite strains. The viscous part is based on a generalized Maxwell model enhanced with nonlinear strain (rate)-dependent relaxation coefficients and times represented by neural networks. The number of Maxwell elements is not determined a priori but adapts automatically during training. Thereby, vCANNs employ L_1 regularization on the Maxwell branches to promote a sparse model. In contrast, traditional models usually specify and fix the number of Maxwell branches before calibrating the material parameters, which requires additional, often labor-intensive tests. vCANNs adopt the computationally very efficient framework of QLV and FLV but generalize these well-established theories to model anisotropic nonlinear viscoelasticity. We demonstrated the ability of vCANNs to learn even challenging viscoelastic behavior of advanced materials by several examples. We also briefly illustrated the ability of vCANNs to process non-mechanical information such as temperature data (or, in other cases also, microstructural or processing data) to predict the behavior of materials under conditions not covered by the training data. We demonstrated that vCANNs could learn the viscoelastic behavior of advanced materials from a database similarly small as the one human experts typically need to calibrate their models. However, vCANNs can learn the material behavior in a fast and fully automated manner, and their application does not require any expert knowledge. These advantages make vCANNs a favorable tool to support the development of new advanced materials in academia and industry.

Of note, vCANNs are not only helpful from a practical perspective but can also promote our theoretical understanding. For example, it is often believed that the generalized Maxwell model with strain-dependent material parameters cannot describe strain-dependent relaxation curves accurately [53]. Interestingly, the application example on the rectus abdominis muscle presented above demonstrates that vCANNs are very well able to accomplish this. These findings raise the question of whether doubts about the capabilities of generalized Maxwell models are mainly a result of difficulties humans face in their proper calibration instead of fundamental shortcomings of this class of models. In such a way, vCANNs can help us with their automated and highly efficient calibration process to understand the actual capabilities and limits of generalized Maxwell models. Exploring this further may be an exciting avenue for future research.

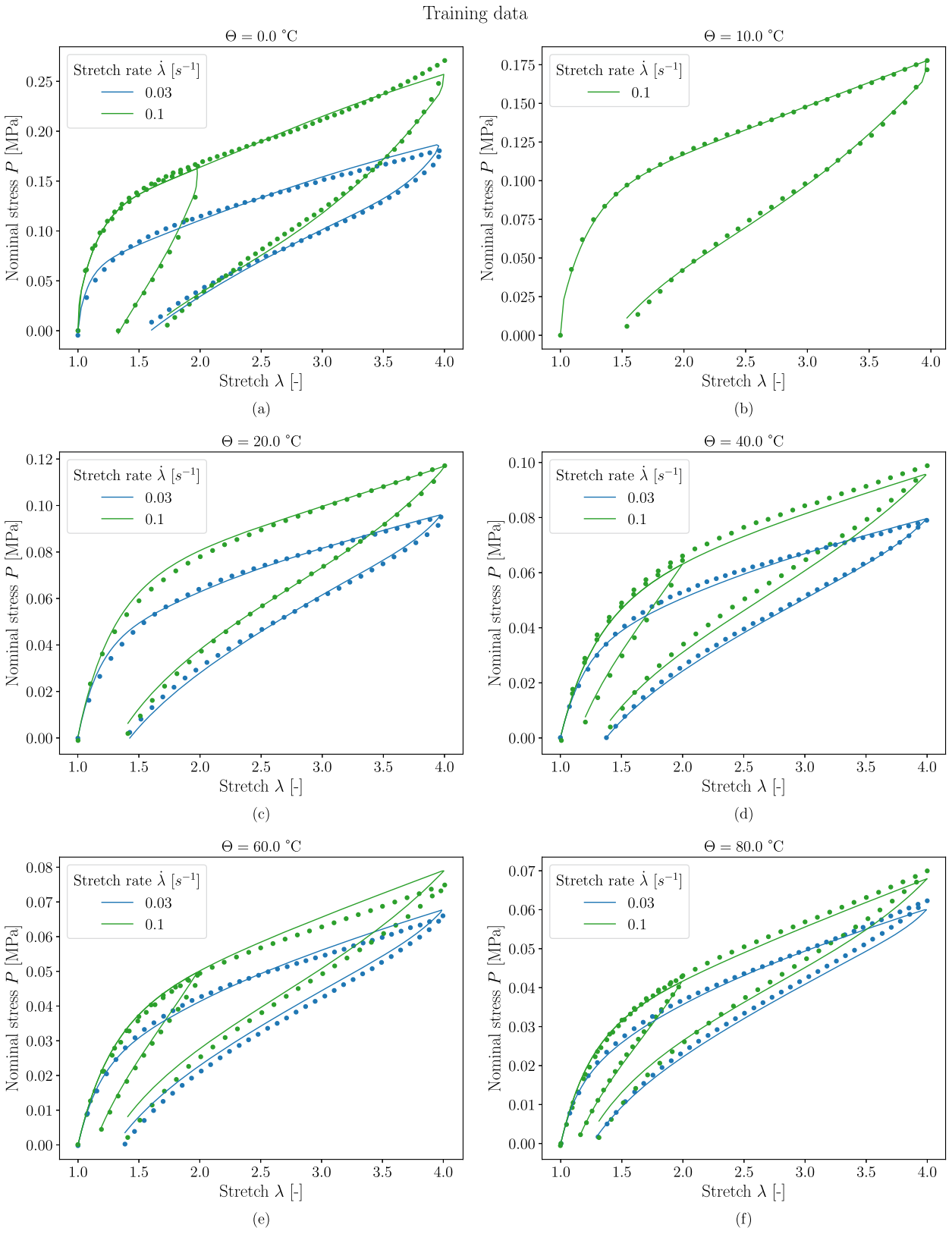

Fig. 10. Performance of the vCANN for VHB 4905: achieved fitting of training data. The dotted lines represent experimental data reproduced from [105]; the solid lines represent the vCANN performance.

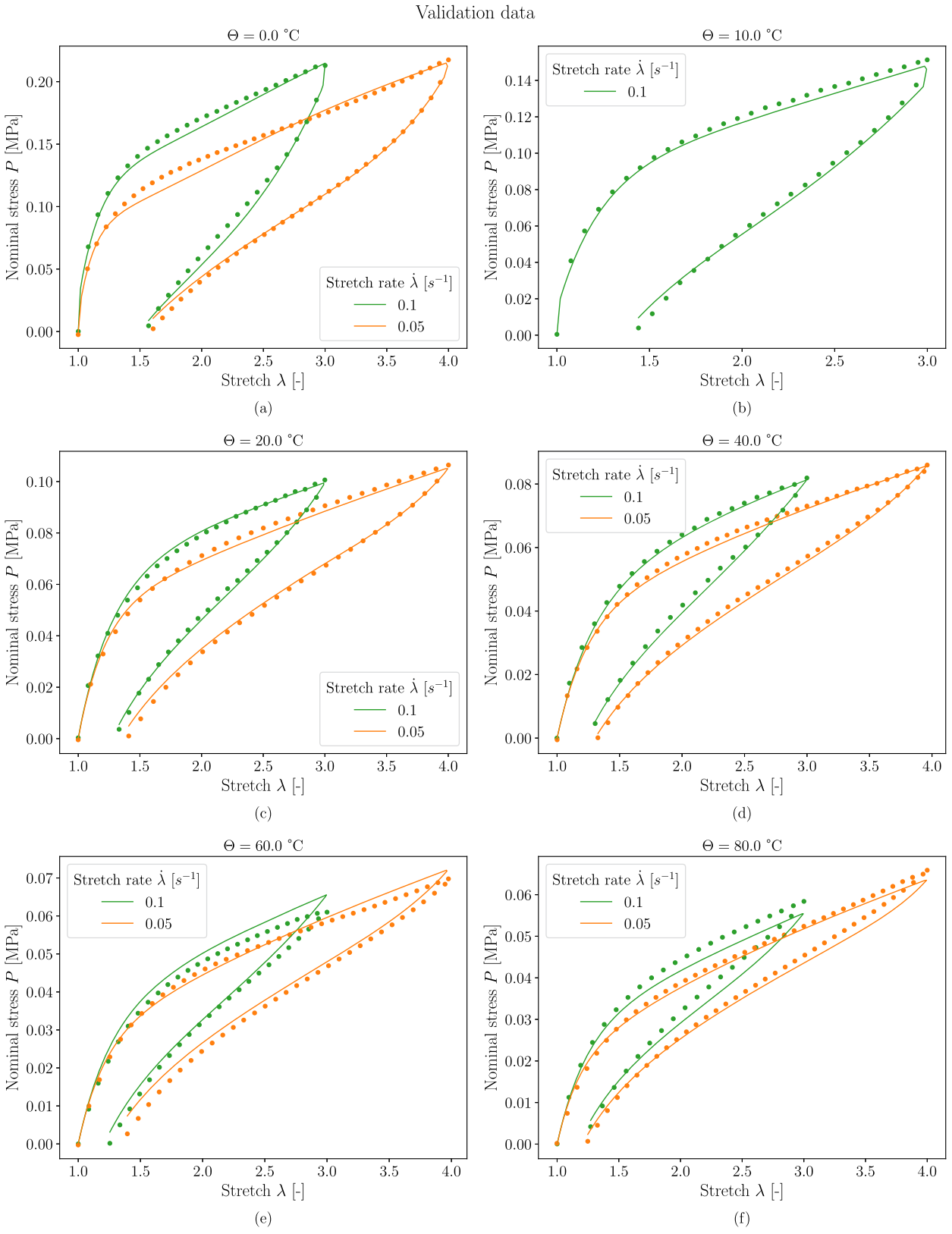

Fig. 11. Performance of the vCANN for VHB 4905: predictive performance on validation data. The dotted lines represent experimental data reproduced from [105]; the solid lines represent the vCANN performance.

CRediT authorship contribution statement

Kian P. Abdolazizi: Conceptualization, Investigation, Methodology, Software, Validation, Visualization, Writing – original draft, Writing – review & editing. **Kevin Linka:** Conceptualization, Methodology, Supervision, Writing – review & editing. **Christian J. Cyron:** Conceptualization, Funding acquisition, Methodology, Supervision, Writing – review & editing.

Declaration of competing interest

The authors declare that they have no known competing financial interests or personal relationships that could have appeared to influence the work reported in this paper.

Data availability

Our source code will be available at https://github.com/ConstitutiveANN/vCANN.

Acknowledgements

K. P. Abdolazizi and C. J. Cyron gratefully acknowledge financial support from TUHH within the I^3-Lab 'Modellgestütztes maschinelles Lernen für die Weichgewebsmodellierung in der Medizin'. We thank Guang Chen (Department of Mechanical Engineering, University of Connecticut) for sharing parts of his code with us, which were not used in the current version of vCANNs but were helpful for us in developing ideas.

Appendix A. Transverse isotropy

To illustrate the proposed constitutive model, we consider a transversely isotropic material. Transversely isotropic materials exhibit one preferred material direction. Material properties remain invariant with respect to rotations about and reflections from the planes orthogonal or parallel to this preferred direction. The preferred direction $\boldsymbol{l}_1$ may be interpreted as the direction of a unidirectional family of fibers embedded into some isotropic matrix. We obtain from Eq. (7) the structural tensors

$$\mathbf{L}_0 = \frac{1}{3}\mathbf{I}, \qquad \mathbf{L}_1 = \boldsymbol{l}_1 \otimes \boldsymbol{l}_1. \tag{A.1}$$

Setting $\mathbf{L}_{r1} = \mathbf{L}_1$, Eq. (7) yields the generalized structural tensors

$$\tilde{\mathbf{L}}_r = \frac{1}{3}\left(1 - w_{r1}\right)\mathbf{I} + w_{r1}\mathbf{L}_1, \quad r = 1, 2, \dots, R. \tag{A.2}$$

The generalized structural tensor Eq. (A.2) describes a transversely isotropic fiber dispersion with rotational symmetry around a mean fiber direction aligned with $\boldsymbol{l}_1$ [106]. Unidirectional alignment requires the uncoupling of the two contributions $\mathbf{I}$ and $\mathbf{L}_1$. Hence, setting $R = 2$, $w_{11} = w_{20} = 0$, and $w_{10} = w_{21} = 1$ results in

$$\tilde{\mathbf{L}}_1 = \frac{1}{3}\mathbf{I}, \qquad \tilde{\mathbf{L}}_2 = \mathbf{L}_1. \tag{A.3}$$

With Eqs. (6) and (20), the generalized invariants are

$$\tilde{I}_1 = \frac{1}{3}\operatorname{tr}(\mathbf{C}), \qquad \tilde{J}_1 = \frac{1}{3}\operatorname{tr}(\operatorname{cof}\mathbf{C}), \qquad \tilde{I}_2 = \operatorname{tr}\left(\mathbf{C}\mathbf{L}_1\right), \qquad \tilde{J}_2 = \operatorname{tr}\left[(\operatorname{cof}\mathbf{C})\mathbf{L}_1\right] \qquad \mathrm{III}_{\mathbf{C}} = \det\mathbf{C} = 1, \tag{A.4}$$

and

$$\tilde{\dot{I}}_1 = \frac{1}{3}\operatorname{tr}\left(\dot{\mathbf{C}}\right), \qquad \tilde{\dot{J}}_1 = \frac{1}{3}\operatorname{tr}\left(\operatorname{cof}\dot{\mathbf{C}}\right), \qquad \tilde{\dot{I}}_2 = \operatorname{tr}\left(\dot{\mathbf{C}}\mathbf{L}_1\right), \qquad \tilde{\dot{J}}_2 = \operatorname{tr}\left[\left(\operatorname{cof}\dot{\mathbf{C}}\right)\mathbf{L}_1\right], \qquad \mathrm{III}_{\dot{\mathbf{C}}} = \det\dot{\mathbf{C}}, \tag{A.5}$$

such that

$$\tilde{\mathcal{I}} = \left\{\tilde{I}_1, \tilde{J}_1, \tilde{I}_2, \tilde{J}_2\right\}, \qquad \tilde{\dot{\mathcal{I}}} = \left\{\tilde{\dot{I}}_1, \tilde{\dot{J}}_1, \tilde{\dot{I}}_2, \tilde{\dot{J}}_2, \mathrm{III}_{\dot{\mathbf{C}}}\right\}, \qquad \mathcal{I} = \tilde{\mathcal{I}} \cup \tilde{\dot{\mathcal{I}}}. \tag{A.6}$$

According to Eq. (12), the instantaneous elastic 2nd Piola–Kirchhoff stress of a transversely isotropic material with unidirectional fiber alignment can be computed by differentiating the strain energy function

$$\Psi = \Psi(\mathcal{I}, \mathbf{f}) \tag{A.7}$$

with respect to $\mathbf{C}$, giving

$$\mathbf{S}^e = -p\mathbf{C}^{-1} + 2\left(\frac{\partial\Psi}{\partial\tilde{I}_1}\mathbf{I} - \frac{\partial\Psi}{\partial\tilde{J}_1}\mathbf{C}^{-2}\right) + 2\left(\frac{\partial\Psi}{\partial\tilde{I}_2}\mathbf{L}_1 - \frac{\partial\Psi}{\partial\tilde{J}_2}\mathbf{C}^{-1}\mathbf{L}_1\mathbf{C}^{-1}\right). \tag{A.8}$$

The reduced relaxation functions Eq. (22) simplify to

$$G_r = G_r(t, \mathcal{I}, \mathbf{f}), \quad r = 1, 2. \tag{A.9}$$

Within the proposed framework of anisotropic nonlinear viscoelasticity, Eqs. (A.8) and (A.9) constitute the most general expressions for the stress and reduced relaxation functions of a transversely isotropic material with unidirectional fiber alignment. For practical applications, it is often useful to uncouple Ψ and G_r with respect to the generalized structural tensors:

$$\Psi = \Psi_1\left(\tilde{I}_1, \tilde{J}_1, \mathbf{f}\right) + \Psi_2\left(\tilde{I}_2, \tilde{J}_2, \mathbf{f}\right), \tag{A.10}$$

$$G_1 = G_1\left(t, \tilde{I}_1, \tilde{J}_1, \tilde{\bar{I}}_1, \tilde{\bar{J}}_1, \mathrm{III}_{\dot{\mathbf{C}}}, \mathbf{f}\right), \qquad G_2 = G_2\left(t, \tilde{I}_2, \tilde{J}_2, \tilde{\bar{I}}_2, \tilde{\bar{J}}_2, \mathrm{III}_{\dot{\mathbf{C}}}, \mathbf{f}\right). \tag{A.11}$$

Uncoupling can significantly accelerate the training process of vCANNs. We can identify Ψ_1 and G_1 with the isotropic strain energy function and reduced relaxation function, respectively. By contrast, Ψ_2 and G_2 represent the anisotropic strain energy function and reduced relaxation function. This example illustrates our proposed framework's versatility and that it includes important classes of anisotropy as special cases.

Appendix B. Numerical time integration

In this section, we provide the derivation of the numerical time-stepping scheme used within the vCANN framework. We are interested in computing the viscous overstresses (Eq. (28))

$$\mathbf{Q}_{r\alpha} = \int_{-\infty}^{t} g_{r\alpha}(\mathcal{I}, \mathbf{f}) \exp\left(-\frac{t-s}{\tau_{r\alpha}(\mathcal{I}, \mathbf{f})}\right) \dot{\mathbf{S}}_r^e \, \mathrm{d}s. \tag{B.1}$$

To this end, we recall the evolution equation of a single Maxwell branch with a strain (rate)-dependent relaxation coefficient and time. The evolution of the viscous overstress $\mathbf{Q}_{r\alpha}$ is governed by the linear ODE of first order with variable coefficients and with some known but otherwise arbitrary initial value $\mathbf{Q}_{r\alpha}^n$ at an arbitrary time point t^n,

$$\dot{\mathbf{Q}}_{r\alpha} + \frac{\mathbf{Q}_{r\alpha}}{\tau_{r\alpha}(\mathcal{I}, \mathbf{f})} = g_{r\alpha}(\mathcal{I}, \mathbf{f}) \dot{\mathbf{S}}_r^e, \quad \mathbf{Q}_{r\alpha}^n = \mathbf{Q}_{r\alpha}(t^n). \tag{B.2}$$

This equation can be solved by a time-stepping scheme after discretizing time into a number of time points t^i. Consider the small time interval $[t^n, t^{n+1}]$ between time points t^n and t^{n+1} with time step size $\Delta t = t^{n+1} - t^n$. For sufficiently small intervals (and assuming a sufficiently smooth problem) Δt, $\tau_{r\alpha}$ and $g_{r\alpha}$ can through the whole time interval be approximated by the average values of its beginning and end point:

$$\bar{\tau}_{r\alpha} = \frac{\left(\tau_{r\alpha}\right)^{n+1} + \left(\tau_{r\alpha}\right)^n}{2}, \qquad \bar{g}_{r\alpha} = \frac{\left(g_{r\alpha}\right)^{n+1} + \left(g_{r\alpha}\right)^n}{2}. \tag{B.3}$$

In a displacement-driven setting, $\bar{\tau}_{r\alpha}$ and $\bar{g}_{r\alpha}$ are known since they depend on the prescribed deformation (rate) at the considered times. With the approximation Eq. (B.3), Eq. (B.2) becomes a linear ODE of first order with constant coefficients and with some known initial value:

$$\dot{\mathbf{Q}}_{r\alpha} + \frac{\mathbf{Q}_{r\alpha}}{\bar{\tau}_{r\alpha}} = \bar{g}_{r\alpha} \dot{\mathbf{S}}_r^e, \quad \mathbf{Q}_{r\alpha}^n = \mathbf{Q}_{r\alpha}(t^n). \tag{B.4}$$

Multiplying both sides of Eq. (B.4) by the integrating factor $\exp(t/\bar{\tau}_{r\alpha})$ and applying the product rule gives

$$\frac{\mathrm{d}}{\mathrm{d}t}\left[\mathbf{Q}_{r\alpha} \exp\left(\frac{t}{\bar{\tau}_{r\alpha}}\right)\right] = \bar{g}_{r\alpha} \dot{\mathbf{S}}_r^e \exp\left(\frac{t}{\bar{\tau}_{r\alpha}}\right). \tag{B.5}$$

Integrating Eq. (B.5) from t^n to t^{n+1} yields

$$\exp\left(\frac{t^{n+1}}{\bar{\tau}_{r\alpha}}\right) \mathbf{Q}_{r\alpha}^{n+1} - \exp\left(\frac{t^n}{\bar{\tau}_{r\alpha}}\right) \mathbf{Q}_{r\alpha}^n = \int_{t^n}^{t^{n+1}} \exp\left(\frac{t}{\bar{\tau}_{r\alpha}}\right) \bar{g}_{r\alpha} \dot{\mathbf{S}}_r^e \, \mathrm{d}t \tag{B.6}$$

which can subsequently be solved for

$$\mathbf{Q}_{r\alpha}^{n+1} = \exp\left(\frac{t^n}{\bar{\tau}_{r\alpha}}\right) \exp\left(-\frac{t^{n+1}}{\bar{\tau}_{r\alpha}}\right) \mathbf{Q}_{r\alpha}^n + \int_{t^n}^{t^{n+1}} \exp\left(\frac{t}{\bar{\tau}_{r\alpha}}\right) \exp\left(-\frac{t^{n+1}}{\bar{\tau}_{r\alpha}}\right) \bar{g}_{r\alpha} \dot{\mathbf{S}}_r^e \, \mathrm{d}t \tag{B.7}$$

$$= \exp\left(-\frac{\Delta t}{\bar{\tau}_{r\alpha}}\right) \mathbf{Q}_{r\alpha}^n + \int_{t^n}^{t^{n+1}} \exp\left(-\frac{t^{n+1} - t}{\bar{\tau}_{r\alpha}}\right) \bar{g}_{r\alpha} \dot{\mathbf{S}}_r^e \, \mathrm{d}t \tag{B.8}$$

$$\approx \exp\left(-\frac{\Delta t}{\bar{\tau}_{r\alpha}}\right)\mathbf{Q}^{n}_{r\alpha} + \exp\left(-\frac{\Delta t}{2\bar{\tau}_{r\alpha}}\right)\bar{g}_{r\alpha}\int_{t^n}^{t^{n+1}}\dot{\mathbf{S}}^{e}_{r}\,\mathrm{d}t \tag{B.9}$$

$$= \exp\left(-\frac{\Delta t}{\bar{\tau}_{r\alpha}}\right)\mathbf{Q}^{n}_{r\alpha} + \exp\left(-\frac{\Delta t}{2\bar{\tau}_{r\alpha}}\right)\bar{g}_{r\alpha}\left[(\mathbf{S}^{e}_{r})^{n+1} - (\mathbf{S}^{e}_{r})^{n}\right] \tag{B.10}$$

which yields a recurrence update formula for the viscous overstress at time t^{n+1}, given we know the state at time t^n. We used the mid-point rule on the integral in Eq. (B.8) approximating the time variable t by $(t^{n+1}-t^n)/2$.

An alternative update formula for the overstress $\mathbf{Q}^{n+1}_{r\alpha}$ can be obtained by approximating $\dot{\mathbf{S}}^{e}_{r} \approx \frac{(\mathbf{S}^{e}_{r})^{n+1}-(\mathbf{S}^{e}_{r})^{n}}{\Delta t}$ directly in Eq. (B.8), which leads to

$$\mathbf{Q}^{n+1}_{r\alpha} = \exp\left(-\frac{\Delta t}{\bar{\tau}_{r\alpha}}\right)\mathbf{Q}^{n}_{r\alpha} + \bar{g}_{r\alpha}\frac{(\mathbf{S}^{e}_{r})^{n+1} - (\mathbf{S}^{e}_{r})^{n}}{\Delta t}\int_{t^n}^{t^{n+1}}\exp\left(-\frac{t^{n+1}-t}{\bar{\tau}_{r\alpha}}\right)\mathrm{d}t \tag{B.11}$$

$$= \exp\left(-\frac{\Delta t}{\bar{\tau}_{r\alpha}}\right)\mathbf{Q}^{n}_{r\alpha} + \frac{\bar{g}_{r\alpha}\bar{\tau}_{r\alpha}}{\Delta t}\left[1-\exp\left(-\frac{\Delta t}{\bar{\tau}_{r\alpha}}\right)\right]\left[(\mathbf{S}^{e}_{r})^{n+1} - (\mathbf{S}^{e}_{r})^{n}\right], \tag{B.12}$$

giving an update formula for the overstress at time t^{n+1}. The two update formulae (B.10) and (B.12) are very similar to common recurrence formulae for the stress update found in the literature [31,107,81]. The major difference to most formulae reported in the literature is that $\bar{\tau}_{r\alpha}$ and $\bar{g}_{r\alpha}$ are not constant but change each time step. In essence, in a discrete time stepping scheme, one solves a different QLV problem in each time step. With Eq. (28), we obtain an update rule for the stress tensor $\mathbf{S}^{n+1}$ at time point t^{n+1}:

$$\mathbf{S}^{n+1} = -\left(p\mathbf{C}^{-1}\right)^{n+1} + \sum_{r=1}^{R}\left((\mathbf{S}^{\infty}_{r})^{n+1} + \sum_{\alpha=1}^{N_r}\mathbf{Q}^{n+1}_{r\alpha}\right). \tag{B.13}$$

The algorithmically consistent linearization of the stress tensor $\mathbf{S}^{n+1}$ is essential for solving nonlinear boundary value problems and preserving a quadratic rate of convergence of iterative solution techniques of Newton's type. The algorithmically consistent tangent of vCANNs

$$\mathbb{C}^{n+1} = 2\frac{\partial \mathbf{S}^{n+1}}{\partial \mathbf{C}^{n+1}}, \tag{B.14}$$

can be derived analytically or computed numerically. The numerical implementation of vCANNs is addressed in detail in a subsequent publication.

Appendix C. Structure learning block

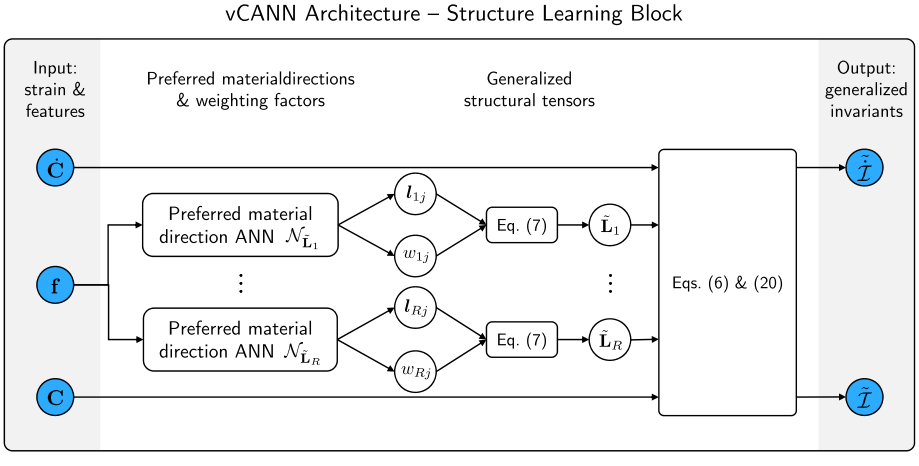

Fig. C.1. Schematic illustration of the structure learning block: The deformation (rate) tensors $\mathbf{C}$, $\dot{\mathbf{C}}$, and the feature vector $\mathbf{f}$ serve as input to the structure learning block. The preferred material directions $\boldsymbol{l}_{rj}$ and scalar weights w_{rj} are learnt from the feature vector $\mathbf{f}$ within dedicated neural networks $\mathcal{N}_{\tilde{\mathbf{L}}_r}$. Inserting the outputs of $\mathcal{N}_{\tilde{\mathbf{L}}_r}$ in Eq. (7) yields the generalized structural tensors $\tilde{\mathbf{L}}_r$. Together with the deformation (rate) tensors $\mathbf{C}$ and $\dot{\mathbf{C}}$, we obtain from Eqs. (6) and (20) the generalized invariants $\tilde{I}$ and $\tilde{\dot{I}}$, respectively. In turn, the generalized invariants $\tilde{I}$ and $\tilde{\dot{I}}$ themselves serve as input to the main part of the vCANN in Fig. 2.

Appendix D. Influence of the time scaling constants $T_{r\alpha}$

Fig. D.1 shows the viscous properties of a vCANN trained with two different initializations of the time scaling constants $T_{r\alpha}$. The vCANN initially comprised ten Maxwell elements and was trained on the high-stretch rate experiments reported in [104]. In

Fig. D.1(a), the vCANN was initialized with $T_{r\alpha}$ uniformly distributed on the logarithmic scale within $[T_{min}, T_{max}] = [10^{-2}, 10^{3}]$, the default choice for all examples in this paper, cf. Appendix I. In Figure D.1(b), the vCANN was initialized with $T_{r\alpha}$ uniformly distributed on the logarithmic scale within the theoretical limits $[T_{min}, T_{max}] = [10^{-10}, 10^{2}]$ s. These theoretical limits were determined based on the longest experiment (ca. 150 s) and the smallest time increment in the training data (ca. $1.9 \cdot 10^{-10}$ s). The learned relaxation times and coefficients are very close to each other, demonstrating the robustness of vCANNs to the initialization of the time scaling constants $T_{r\alpha}$. Note that in Fig. D.1(a), the vCANN keeps four out of ten Maxwell elements after training, in Fig. D.1(b), three out of ten Maxwell elements are kept. However, the relaxation coefficient g_7 of the additional Maxwell element in Fig. D.1(a) is close to zero, thus almost negligible. The R^2 values of the stress responses of both initializations are close to one, indicating a precise fit and prediction of the training and validation data.

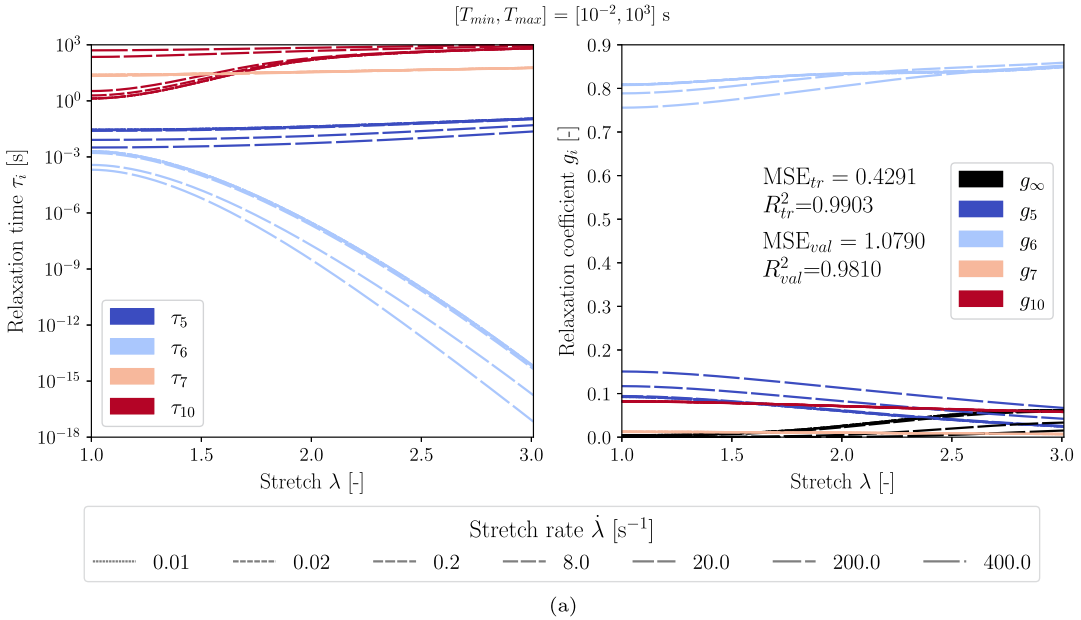

(a)

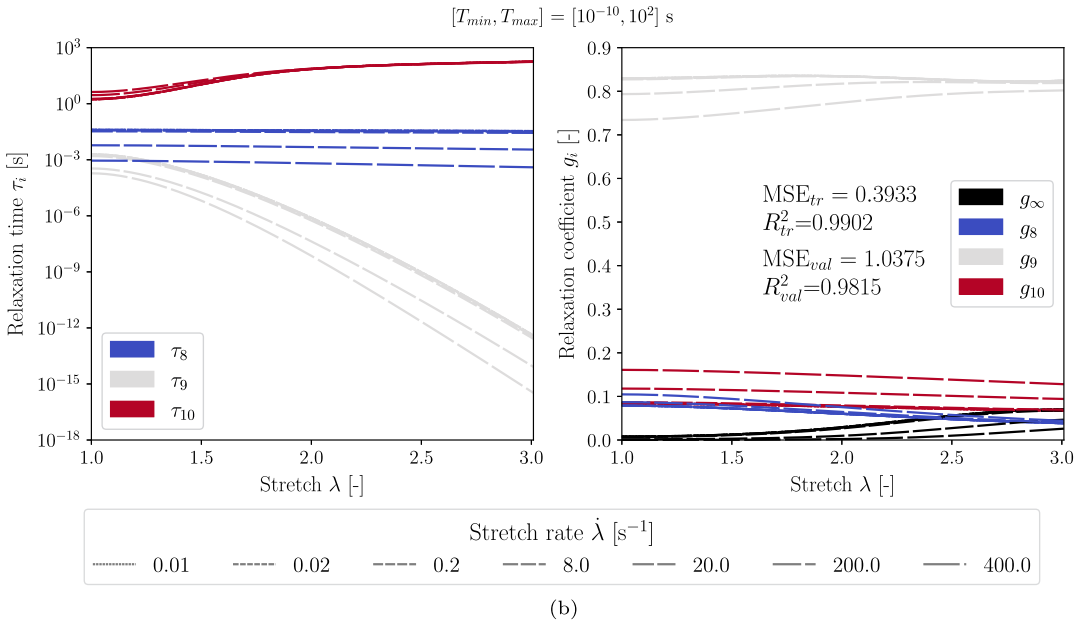

(b)

Fig. D.1. Relaxation times (left) and coefficients (right) of a vCANN trained with the data of the high-stretch rate experiments reported in [104] and initialized with different time scaling constants $[T_{min}, T_{max}]$. Comparing the mean squared errors (MSE) and coefficients of determination (R^2) of the stress responses indicates that the vCANN fits and predicts the training and validation set equally well, regardless of the time scaling initialization. Quantities evaluated on the training and validation set are indicated with the subscripts $(\cdot)_{tr}$ and $(\cdot)_{val}$, respectively. The color of the lines indicates the Maxwell element and the dash pattern indicates the stretch rate. (a) The vCANN was initialized with $[T_{min}, T_{max}] = [10^{-2}, 103]$ s, the default for all examples in this paper. Four of the initial 10 Maxwell elements were kept after training. (b) The vCANN was initialized with the theoretical limits $[T_{min}, T_{max}] = [10^{-10}, 102]$ s. Three of the initial 10 Maxwell elements were kept after training.

Appendix E. Representative loss curves and influence of the sparsity parameter Λ

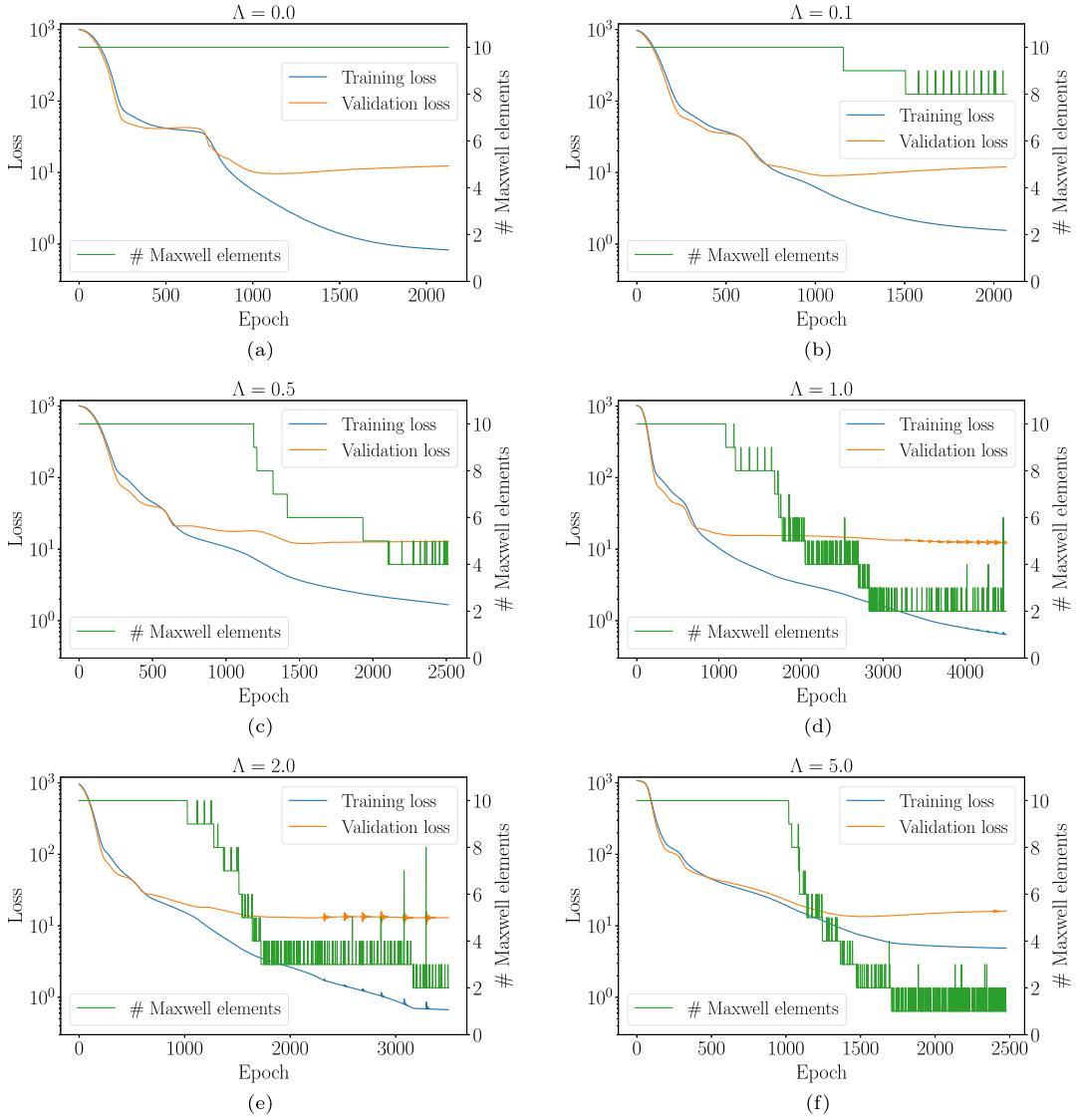

Fig. E.1. Training and validation loss and the number of active Maxwell elements over the training course for increasing values of Λ. The plots show that the vCANN trains well. The oscillations of the losses are associated with occasional eliminations and additions of Maxwell elements in the architecture. As expected, these eliminations and additions require substantial weight adjustments. Beyond $\Lambda = 2$ the vCANN becomes too sparse, which significantly increases the training and validation loss. The vCANN was trained on the VHB 4910 data [100].

Appendix F. Material parameters of the Ogden and HGO model for synthetic data generation

Table F.1
Isotropic and anisotropic elastic material parameters.

μ_1	α_1	k_1	k_2
0.3	3.7	0.3	0.4

Table F.2
Isotropic (Ogden model – OG) and anisotropic (Holzapfel–Gasser–Ogden model – HGO) viscoelastic material parameters.

$\hat{\tau}_{a,1}^{\mathrm{OG}}$	$\hat{\tau}_{b,1}^{\mathrm{OG}}$	$\hat{g}_{a,1}^{\mathrm{OG}}$	$\hat{g}_{b,1}^{\mathrm{OG}}$	$\hat{\tau}_{a,2}^{\mathrm{OG}}$	$\hat{\tau}_{b,2}^{\mathrm{OG}}$	$\hat{g}_{a,2}^{\mathrm{OG}}$	$\hat{g}_{b,2}^{\mathrm{OG}}$	$\hat{\tau}_{a,2}^{\mathrm{HGO}}$	$\hat{\tau}_{b,2}^{\mathrm{HGO}}$	$\hat{g}_{a,2}^{\mathrm{HGO}}$	$\hat{g}_{b,2}^{\mathrm{HGO}}$
20.0	-7.0	0.4	-2.8	1.0	4.0	0.1	-2.8	10.0	0.7	0.8	-1.1

Appendix G. Side-by-side comparison of simulation results by vCANNs and classical models from the literature

In Sec. 4, we have compared the simulation results of vCANNs to those of several classical constitutive models. For the reader's convenience, we provide side-by-side comparisons of the vCANNs' and the classical constitutive models' simulation results.

G.1. Passive viscoelastic response of the abdominal muscle, Sec. 4.2

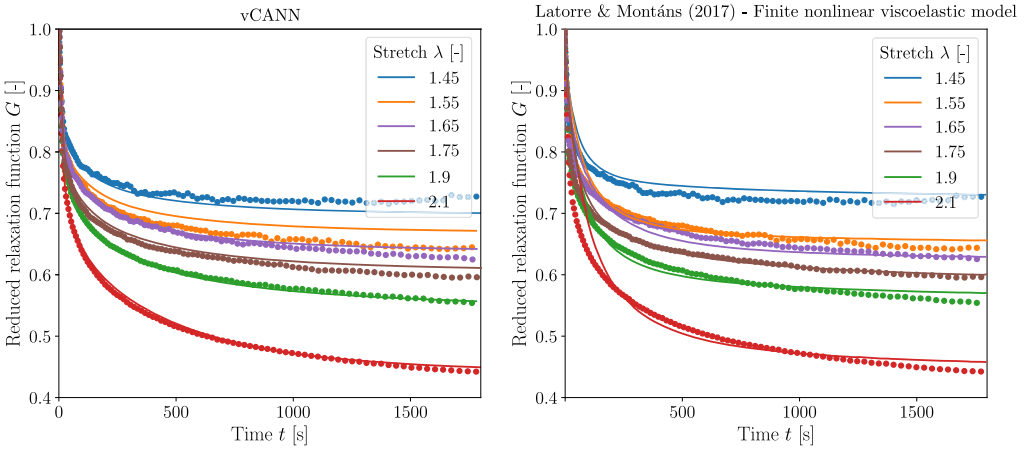

Fig. G.1. Comparison between the simulation results of the vCANN (left) and those of the classical finite nonlinear viscoelastic constitutive model (right) proposed by Latorre & Montáns [50] (reproduced from Fig. 5 therein) for the uniaxial relaxation response of the leporine rectus abdominis muscle. The solid lines represent simulation results. The dotted lines represent experimental data. The constitutive model of Latorre & Montáns was fitted against all six relaxation curves. The vCANN was trained with the relaxation curves corresponding $\lambda = 1.45, 1.55, 1.9, 2.1$ and validated with the relaxation curves corresponding to $\lambda = 1.65$ and 1.75.

G.2. Viscoelastic modeling of VHB 4910, Sec. 4.3

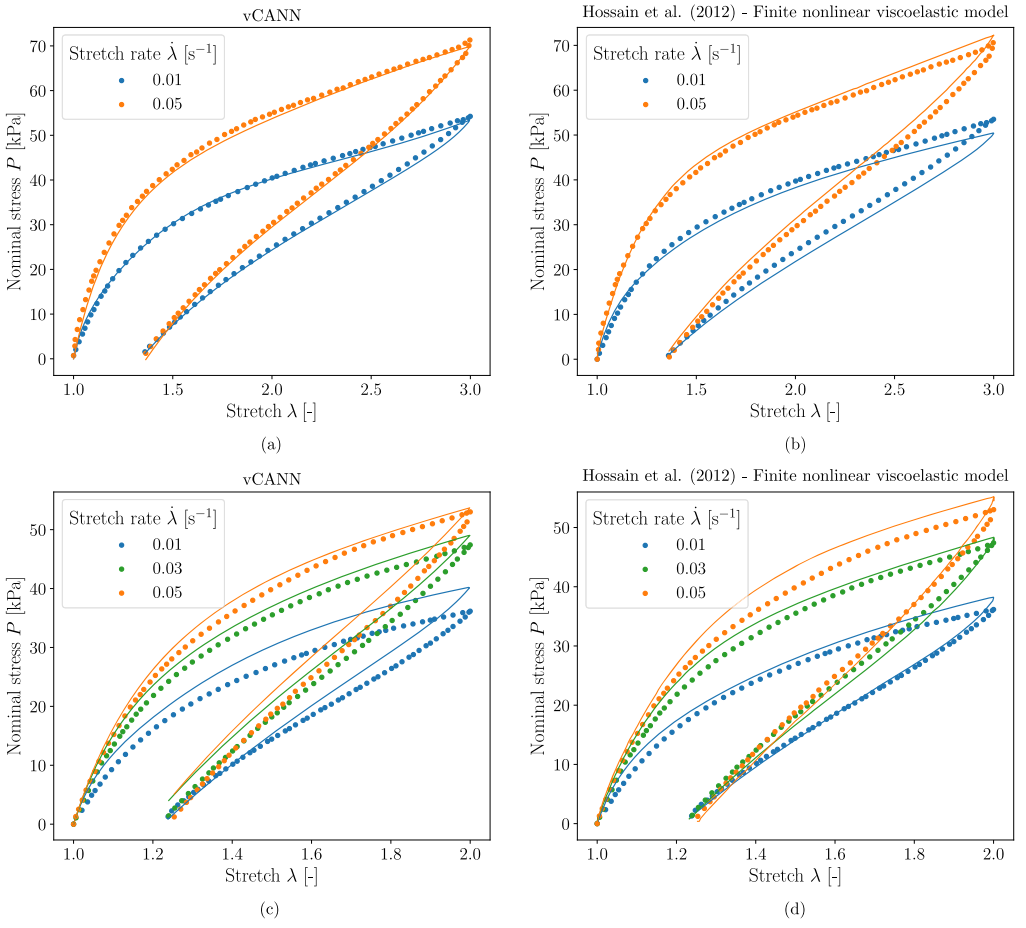

Fig. G.2. Comparison between the simulation results of the vCANN (left column) and the simulation results of the classical finite nonlinear viscoelastic constitutive model (right column) proposed by Hossain et al. [100] (reproduced from Figs. 9–12 therein) for uniaxial loading and unloading. The solid lines represent simulation results. The dotted lines represent experimental data of VHB 4910. The elastic material parameters of the finite nonlinear viscoelastic model proposed by Hossain et al. were separately identified using the data from a multi-step relaxation test, which are not shown here. The viscous material parameters have been separately identified from the experimental data in Fig. G.2(b).

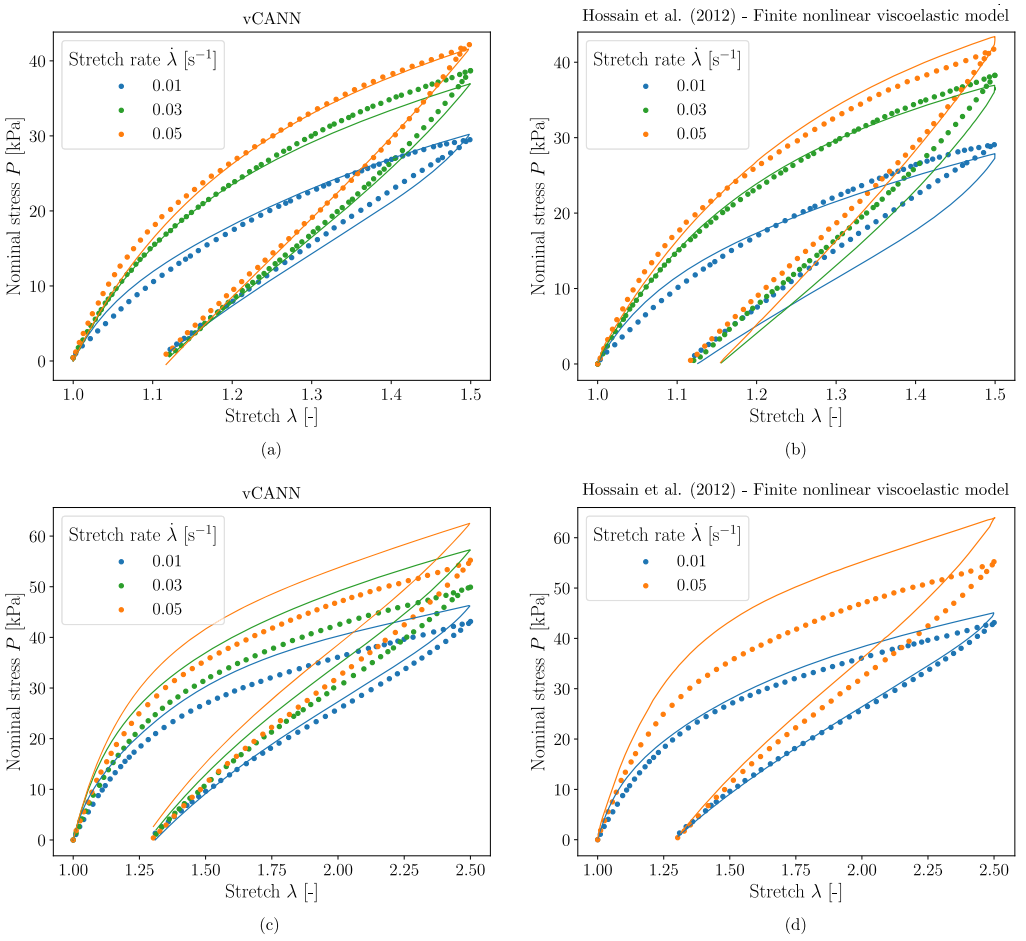

Fig. G.3. Comparison between the simulation results of the vCANN (left column) and the simulation results of the classical finite nonlinear viscoelastic constitutive model (right column) proposed by Hossain et al. [100] (reproduced from Figs. 9–12 therein) for uniaxial loading and unloading. The solid lines represent simulation results. The dotted lines represent experimental data of VHB 4910. The elastic material parameters of the finite nonlinear viscoelastic model proposed by Hossain et al. [100] were separately identified using the data from a multi-step relaxation test, which are not shown here. The viscous material parameters have been separately identified from the experimental data in Fig. G.2(b). No simulation results for $\lambda = 2.5$ at $\dot{\lambda} = 0.03$ s^{-1} were reported in [100].

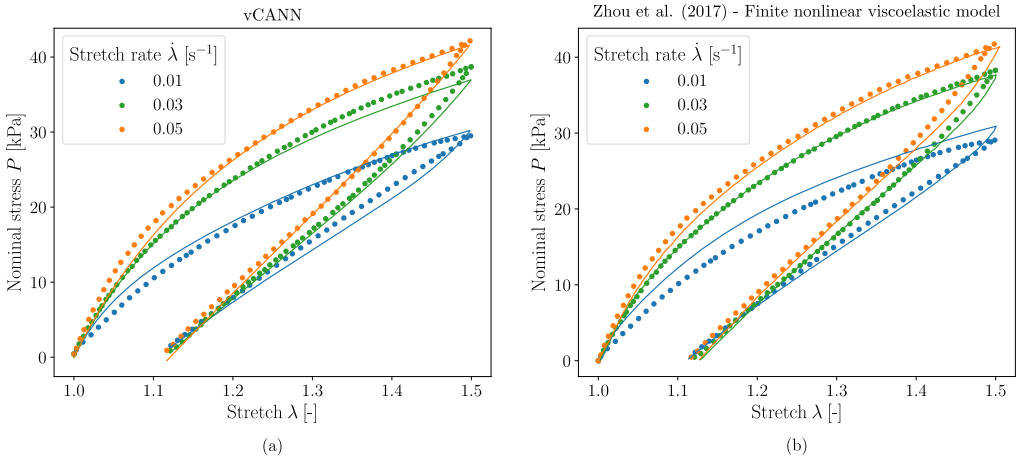

Fig. G.4. Comparison between the simulation results of the vCANN (left column) and the simulation results of the classical finite nonlinear viscoelastic constitutive model (right column) proposed by Zhou et al. [103] (reproduced from Fig. 5(d) therein) for uniaxial loading-unloading data of VHB 4910 reported in [100]. The solid lines represent simulation results. The dotted lines represent experimental data. The elastic material parameters of the finite nonlinear viscoelastic model proposed by Zhou et al. [103] have been separately identified from quasi-static uniaxial tensile experiments, which are not shown here. The viscous material parameters have been identified from all loading-unloading experiments shown in Figs. G.5 and G.4. No simulation results for $\lambda = 2.5$ were reported in [103].

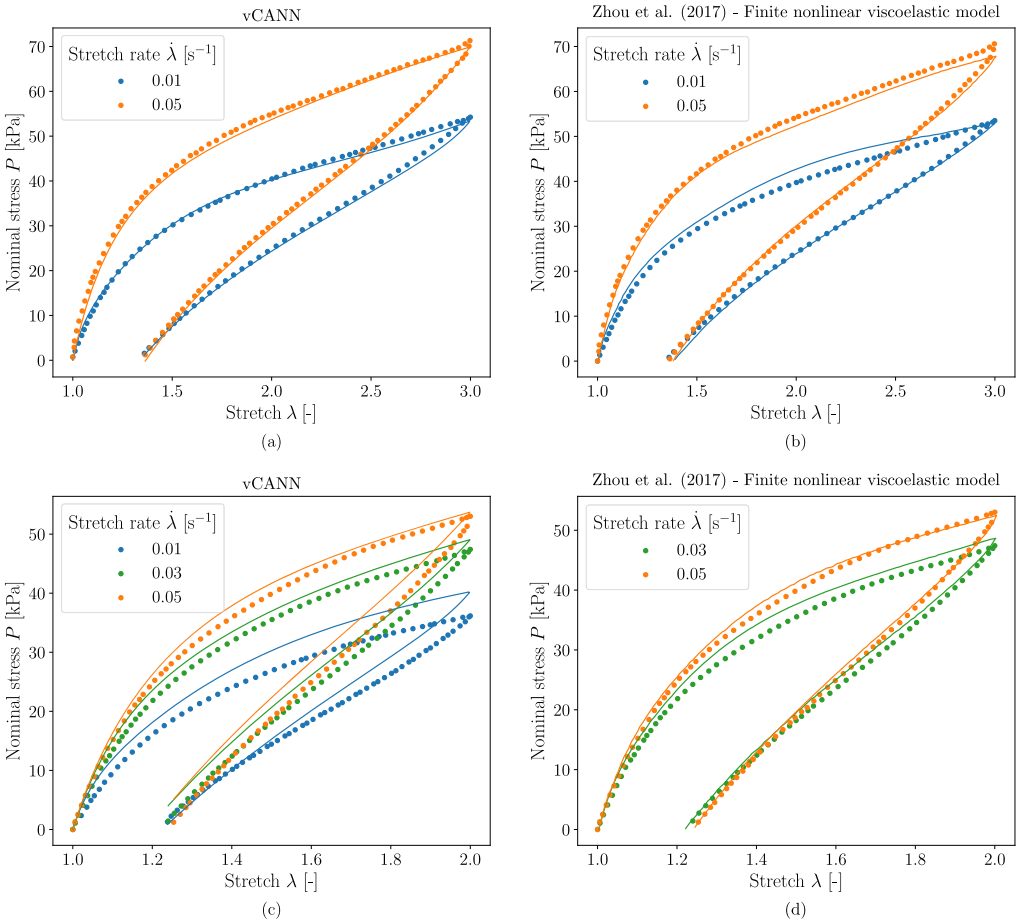

Fig. G.5. Comparison between the simulation results of the vCANN (left column) and those of the classical finite nonlinear viscoelastic constitutive model (right column) proposed by Zhou et al. [103] (reproduced from Figs. 5(b) and 5(c) therein) for uniaxial loading-unloading data of VHB 4910 reported in [100]. The solid lines represent simulation results. The dotted lines represent experimental data. The elastic material parameters of the finite nonlinear viscoelastic model proposed by Zhou et al. [103] have been separately identified from quasi-static uniaxial tensile experiments, which are not shown here. The viscous material parameters have been identified from all loading-unloading experiments shown in Figs. G.5 and G.4. No simulation results for $\lambda = 2$ at $\dot{\lambda} = 0.01$ s^{-1} were reported in [103].

G.3. Blast load analysis of polyvinyl butyral, Sec. 4.4

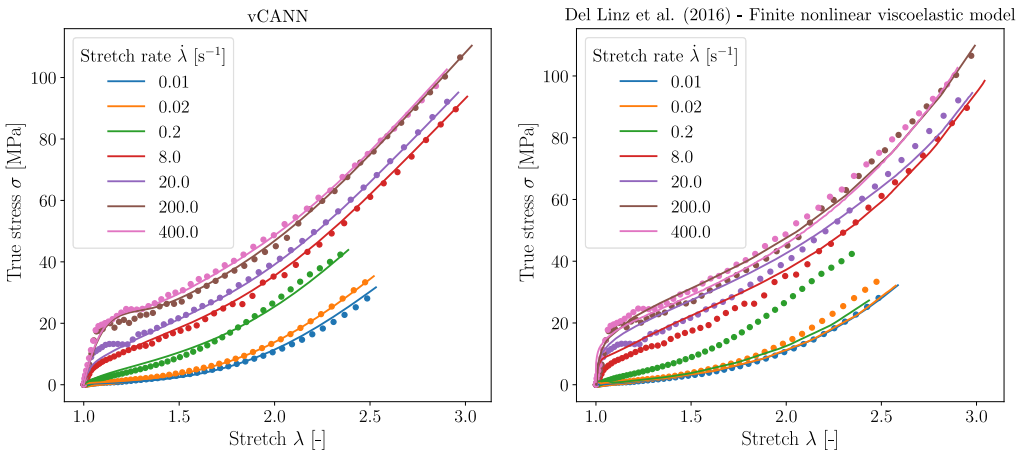

Fig. G.6. Comparison between the simulation results of the vCANN (left) and the simulation results of the classical finite nonlinear viscoelastic constitutive model (left) proposed by [104] (reproduced from Figs. 16 and 17 therein) for high strain rate experiments of Polyvinyl Butyral. The solid lines represent simulation results. The dotted lines represent experimental data. No simulation results for the stretch rates $\dot{\lambda} = 0.1$ and 60.0 s^{-1} were reported in [104].

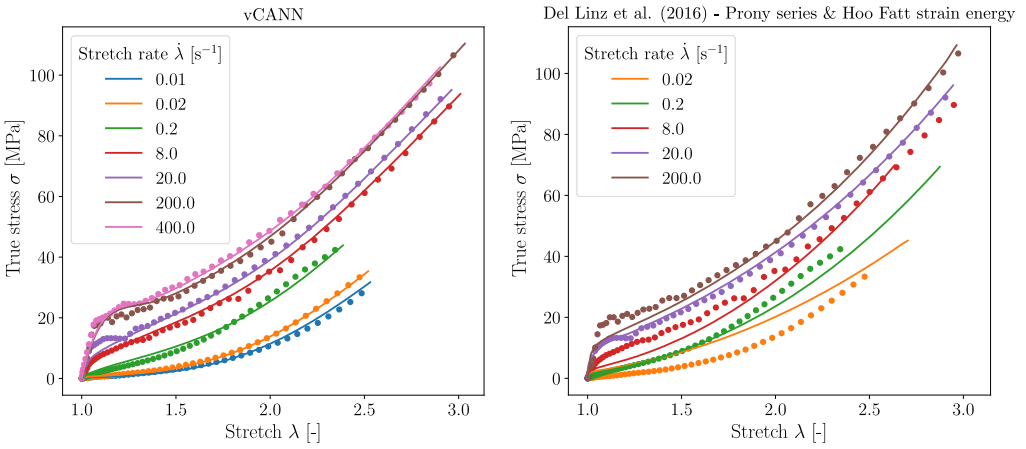

Fig. G.7. Comparison between the simulation results of the vCANN (left) and the simulation results of the Prony series model with Hoo Fatt's strain energy function (right) proposed by [104] (reproduced from Figs. 12 and 13 therein) for high strain rate experiments of Polyvinyl Butyral. The solid lines represent simulation results. The dotted lines represent experimental data. No simulation results for the stretch rates $\dot{\lambda} = 0.01, 0.1, 60.0$, and 400.0 s^{-1} were reported in [104]. Note that the figure on the right essentially shows the simulation results of two different models. One was fitted to the low stretch rate regime (up to $\dot{\lambda} = 8$ s^{-1}) and one to the high stretch rate regime ($\dot{\lambda} = 20$ s^{-1} and above).

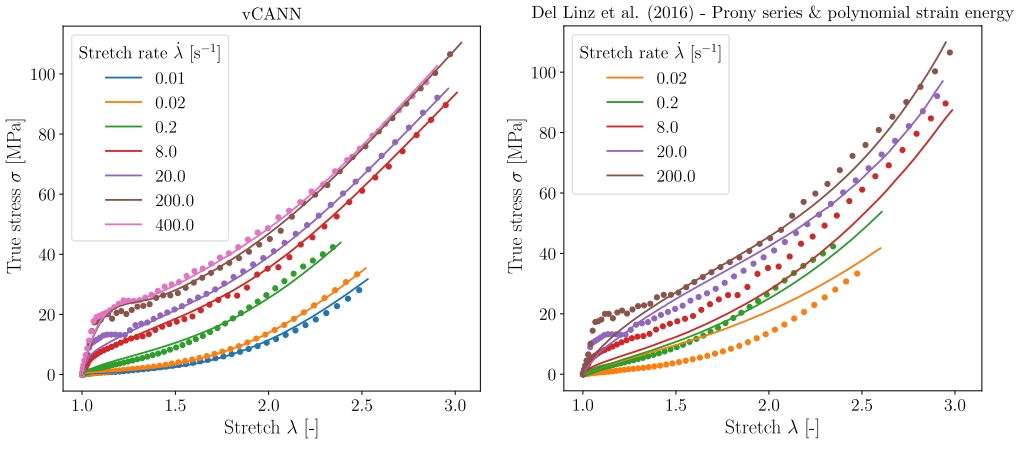

Fig. G.8. Comparison between the simulation results of the vCANN (left) and the simulation results of the Prony series model with polynomial strain energy function (right) proposed by [104] (reproduced from Figs. 14 and 15 therein) for high strain rate experiments of Polyvinyl Butyral. The solid lines represent simulation results. The dotted lines represent experimental data. No simulation results for the stretch rates $\dot{\lambda} = 0.01, 0.1, 60.0$, and 400.0 s^{-1} were reported in [104]. Note that the figure on the right essentially shows the simulation results of two different models. One was fitted to the low stretch rate regime (up to $\dot{\lambda} = 8$ s^{-1}) and one to the high stretch rate regime ($\dot{\lambda} = 20$ s^{-1} and above).

Appendix H. Extrapolation behavior for VHB 4905

To illustrate the extrapolation behavior of vCANNs, we trained a vCANN on the loading-unloading data of VHB 4905 at different temperature levels Θ, maximum stretch amplitudes λ, and stretch rates $\dot{\lambda}$. However, no data at the temperature levels 0 °C and 80 °C were used to train the vCANN. Thus, to predict the stress response at these temperature levels, the vCANN had to extrapolate. Figure H.1(a) illustrates which tuples of $(\lambda, \dot{\lambda}, \Theta)$ have been used for training and validation (extrapolation). In contrast, in Sec. 4.5, the vCANN had to interpolate during validation, Fig. H.1(b).

Figure H.2 shows the training and extrapolation results of the vCANN. The fit of the training data is very accurate. Similarly, the predictions at 80 °C are accurate for the stretch rates 0.03 s^{-1} and 0.05 s^{-1}. The prediction at 80 °C for the stretch rate 0.1 s^{-1} is less accurate. The deviation from the experimental data can be attributed to the S-shape of the loading-unloading curve. The vCANN has never received any S-shaped loading-unloading curves during training, cf. Figs. H.2(b)–(e). At 0 °C, the vCANN predicts stress values that are slightly lower than the experimental values. This shift can be attributed to the fact that a temperature increase from 60 °C to 80 °C hardly changes the stress amplitude of the experimental curves, Figs. H.2(e)–(f). However, the vCANN extrapolates from the training data the effect of the temperature increase from 40 °C to 60 °C, which results in a significant decrease in the stress amplitude, Figs. H.2(d)–(e). Nevertheless, considering that the nonlinear temperature dependence of the stress response is most prevalent outside

of the training data, the predictions for the extrapolation data are very satisfactory. In particular, the vCANN extrapolates the stress response in a physically plausible manner. In contrast, standard neural networks often show abrupt flattening or severe oscillations outside the training data regime [108].

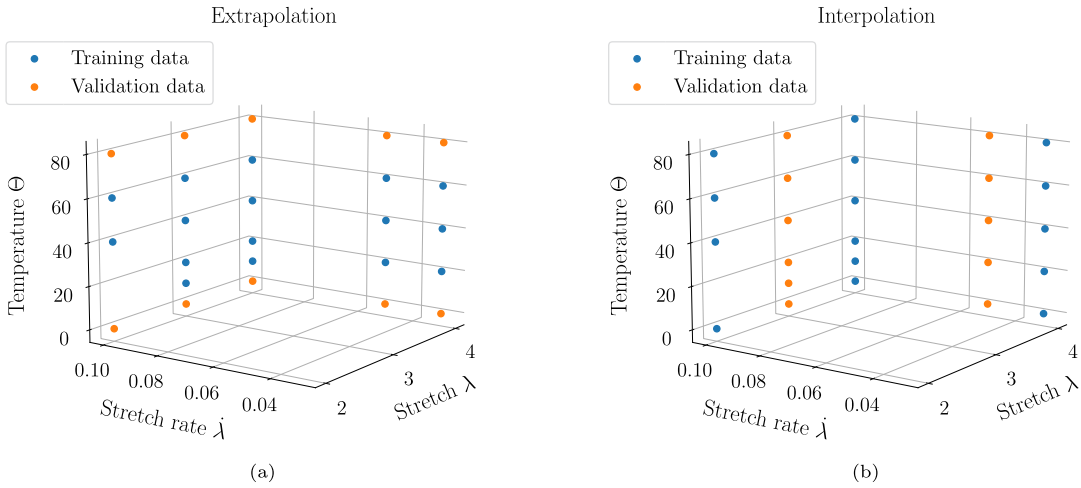

Fig. H.1. Tuples of $(\lambda, \dot{\lambda}, \Theta)$ used for training (blue) and validation (orange). (a) Extrapolation: The validation tuples lie outside of the convex hull of the training tuples. Thus, the vCANN extrapolates during validation. (b) Interpolation: The validation tuples used in Sec. 4.5 lie within the convex hull of the training tuples. Thus, the vCANN interpolates during validation.

Appendix I. Model training and hyperparameters

In the following we list the vCANNs trained in Sec. 4 together with their hyperparameters. The selection of activation functions is discussed in Sec. 3. For training the vCANNs, we used the mean squared error (MSE) between the actual stress response and the one estimated by the vCANN as the loss function. The gradients of the loss with respect to model parameters are calculated by the backpropagation algorithm using automatic differentiation. The training was terminated based on early stopping. All weights and biases were initialized with Glorot/Xavier uniform initializer and zeros, respectively. No regularization (weight decay) was applied to the weights and biases during training. No dropout layers were used. All vCANNs were trained with Adam optimizer ($\beta_1 = 0.9$, $\beta_2 = 0.999$, $\varepsilon = 10^{-7}$).

I.1. Anisotropic viscoelasticity with synthetic data, Sec. 4.1

The material is transversely isotropic, exhibits strain-dependent but no strain rate-dependent viscous effects, and has no notable features ($\mathbf{f} = \mathbf{0}$). Thus, according to Eqs. (A.10) and (A.11), the vCANNs is given by (see also Table I.1)

$$\Psi = \Psi_1\left(\tilde{I}_1, \tilde{J}_1\right) + \Psi_2(\tilde{I}_2, \tilde{J}_2)\,, \qquad G_1 = G_1\left(t, \tilde{I}_1, \tilde{J}_1\right), \qquad G_2 = G_2\left(t, \tilde{I}_2, \tilde{J}_2\right). \tag{I.1}$$

Table I.1
Hyperparameters of the vCANN from Sec. 4.1.

Hyperparameter	Value
General	
Learning rate	0.001
Sparsity penalty parameter Λ	0.001
Instantaneous elastic stress (CANN)	
Convex	Yes
Number of neurons per hidden layer (Ψ_1)	$\{32, 32, 32\}$
Number of neurons per hidden layer (Ψ_2)	$\{32, 32, 32\}$
Reduced relaxation functions	
Maximal number of Maxwell elements N_1^{max}	5
Maximal number of Maxwell elements N_2^{max}	5
Time scaling $[T_{min}, T_{max}]$	$[10^{-2}, 10^{3}]$ s
Number of neurons per hidden layer of $\mathcal{N}_{\tau_{1\alpha}}$	$\{32, 32, 16\}$
Number of neurons per hidden layer of $\mathcal{N}_{g_{1\alpha}}$	$\{32, 32, 16\}$
Number of neurons per hidden layer of $\mathcal{N}_{\tau_{2\alpha}}$	$\{32, 32, 16\}$
Number of neurons per hidden layer of $\mathcal{N}_{g_{2\alpha}}$	$\{32, 32, 16\}$

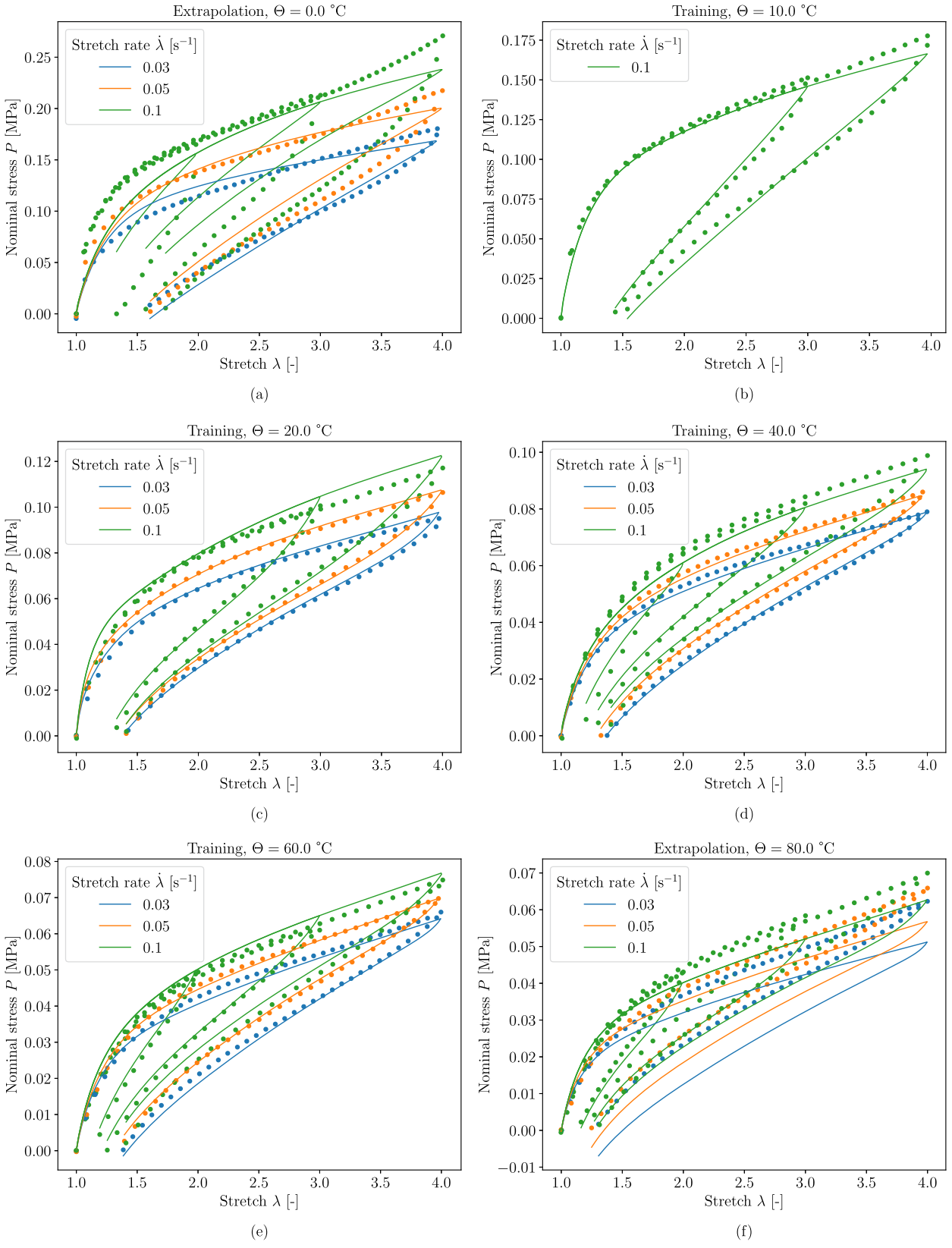

Fig. H.2. Performance of the vCANN for VHB 4905; (a) and (f): predictive performance on validation data during extrapolation, (b)–(e): achieved fitting of training data. The dotted lines represent experimental data reproduced from [105]; the solid lines represent the vCANN's simulation results.

I.2. Passive viscoelastic response of the abdominal muscle, Sec. 4.2

The material is isotropic, exhibits strain-dependent but no strain rate-dependent viscous effects, and has no notable features ($\mathbf{f} = \mathbf{0}$). Thus, according to Eqs. (A.10) and (A.11), the vCANNs is given by (see also Table I.2)

$$\Psi = \Psi_1\left(\tilde{I}_1, \tilde{J}_1\right), \qquad G_1 = G_1\left(t, \tilde{I}_1, \tilde{J}_1\right). \tag{I.2}$$

Table I.2
Hyperparameters of the vCANN from Sec. 4.2.

Hyperparameter	Value
General	
Learning rate	0.001
Sparsity penalty parameter Λ	0.0002
Instantaneous elastic stress (CANN)	
Convex	Yes
Number of neurons per hidden layer	$\{32, 32, 16\}$
Reduced relaxation functions	
Maximal number of Maxwell elements N_1^{max}	10
Time scaling $[T_{min}, T_{max}]$	$[10^{-2}, 10^{3}]$ s
Number of neurons per hidden layer of $\mathcal{N}_{\tau_{1\alpha}}$	$\{32, 32, 16\}$
Number of neurons per hidden layer of $\mathcal{N}_{g_{1\alpha}}$	$\{32, 32, 16\}$

I.3. Viscoelastic modeling of VHB 4910, Sec. 4.3

The material is isotropic, exhibits strain-dependent but no strain rate-dependent viscous effects, and has no notable features ($\mathbf{f} = \mathbf{0}$). Thus, according to Eqs. (A.10) and (A.11), the vCANNs is given by (see also Table I.3)

$$\Psi = \Psi_1\left(\tilde{I}_1, \tilde{J}_1\right), \qquad G_1 = G_1\left(t, \tilde{I}_1, \tilde{J}_1\right). \tag{I.3}$$

Table I.3
Hyperparameters of the vCANN from Sec. 4.3.

Hyperparameter	Value
General	
Learning rate	0.001
Sparsity penalty parameter Λ	1.0
Instantaneous elastic stress (CANN)	
Convex	Yes
Number of neurons per hidden layer	$\{8, 8, 6\}$
Reduced relaxation functions	
Maximal number of Maxwell elements N_1^{max}	10
Time scaling $[T_{min}, T_{max}]$	$[10^{-2}, 10^{3}]$ s
Number of neurons per hidden layer of $\mathcal{N}_{\tau_{1\alpha}}$	$\{16, 16, 8\}$
Number of neurons per hidden layer of $\mathcal{N}_{g_{1\alpha}}$	$\{16, 16, 8\}$

I.4. Blast load analysis of polyvinyl butyral, Sec. 4.4

The material is isotropic, exhibits strain-dependent and strain rate-dependent viscous effects, and has no notable features ($\mathbf{f} = \mathbf{0}$). Thus, according to Eqs. (A.10) and (A.11), the vCANNs is given by (see also Table I.4)

$$\Psi = \Psi_1\left(\tilde{I}_1, \tilde{J}_1\right), \qquad G_1 = G_1\left(t, \tilde{I}_1, \tilde{J}_1, \tilde{\tilde{I}}_1, \tilde{\tilde{J}}_1, \mathrm{III}_{\boldsymbol{C}}\right). \tag{I.4}$$

Table I.4
Hyperparameters of the vCANN from Sec. 4.4.

Hyperparameter	Value
General	
Learning rate	0.0014
Sparsity penalty parameter Λ	0.025
Instantaneous elastic stress (CANN)	
Convex	Yes
Number of neurons per hidden layer	$\{16, 16, 16\}$
Reduced relaxation functions	
Maximal number of Maxwell elements N_1^{max}	10
Time scaling $[T_{min}, T_{max}]$	$[10^{-2}, 10^{3}]$ s
Number of neurons per hidden layer of $\mathcal{N}_{\tau_{1\alpha}}$	$\{24, 24, 24\}$
Number of neurons per hidden layer of $\mathcal{N}_{g_{1\alpha}}$	$\{24, 24, 24\}$

I.5. Thermo-viscoelastic modeling of VHB 4905 data, Sec. 4.5

The material is isotropic, exhibits strain-dependent but no strain rate-dependent viscous effects, and its mechanical behavior is significantly temperature-dependent ($\mathbf{f} = [\Theta]^{\mathrm{T}}$). Thus, according to Eqs. (A.10) and (A.11), the vCANNs is given by (see also Table I.5)

$$\Psi = \Psi_1\left(\tilde{I}_1, \tilde{J}_1, \Theta\right), \qquad G_1 = G_1\left(t, \tilde{I}_1, \tilde{J}_1, \Theta\right). \tag{I.5}$$

Table I.5
Hyperparameters of the vCANN from Sec. 4.5.

Hyperparameter	Value
General	
Learning rate	0.0005
Sparsity penalty parameter Λ	0.0001
Instantaneous elastic stress (CANN)	
Convex	Yes
Number of neurons per hidden layer	$\{32, 32, 16\}$
Reduced relaxation functions	
Maximal number of Maxwell elements N_1^{max}	10
Time scaling $[T_{min}, T_{max}]$	$[10^{-2}, 10^{3}]$ s
Number of neurons per hidden layer of $\mathcal{N}_{\tau_{1\alpha}}$	$\{32, 32, 16\}$
Number of neurons per hidden layer of $\mathcal{N}_{g_{1\alpha}}$	$\{32, 32, 16\}$

Appendix J. VHB 4910 data

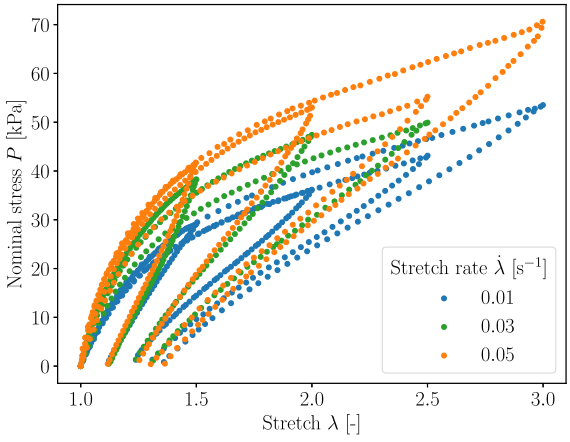

Fig. J.1. Uniaxial loading-unloading data of VHB 4910 taken from [100]. Note that for a given stretch rate $\dot{\lambda}$, the loading curves should coincide for all maximal stretches. However, for example, the loading curve with $\lambda_{max} = 2.5$ and stretch rate $\dot{\lambda} = 0.05$ s^{-1} does not coincide with the other loading curves at $\dot{\lambda} = 0.05$ s^{-1}. This suggests measurement errors or variations of the material samples not uncommon in mechanical testing. Such errors and variations in the data necessarily limit the extent to which a model can capture all the data.

References

[1] A.F.M. Saiful-Amin, Alexander Lion, S. Sekita, Yoshiaki Okui, Nonlinear dependence of viscosity in modeling the rate-dependent response of natural and high damping rubbers in compression and shear: experimental identification and numerical verification, Int. J. Plast. 22 (9) (2006) 1610–1657.
[2] Peter Haupt, Konstantin Sedlan, Viscoplasticity of elastomeric materials: experimental facts and constitutive modelling, Arch. Appl. Mech. 71 (2–3) (2001) 89–109.
[3] Alexander Lion, A constitutive model for carbon black filled rubber: experimental investigations and mathematical representation, Contin. Mech. Thermodyn. 8 (3) (1996) 153–169.
[4] Dominique P. Pioletti, Lalao R. Rakotomanana, On the independence of time and strain effects in the stress relaxation of ligaments and tendons, J. Biomech. 33 (12) (2000) 1729–1732.
[5] Frances M. Davis, Raffaella De Vita, A nonlinear constitutive model for stress relaxation in ligaments and tendons, Ann. Biomed. Eng. 40 (12) (2012) 2541–2550.
[6] Sarah E. Duenwald, Ray Vanderby, Roderic S. Lakes, Viscoelastic relaxation and recovery of tendon, Ann. Biomed. Eng. 37 (6) (2009) 1131–1140.
[7] Christine E. Miller, Chandra L. Wong, Trabeculated embryonic myocardium shows rapid stress relaxation and non-quasi-linear viscoelastic behavior, J. Biomech. 33 (5) (2000) 615–622.
[8] Paolo.P. Provenzano, Roderic S. Lakes, David T. Corr, Ray Vanderby, Application of nonlinear viscoelastic models to describe ligament behavior, Biomech. Model. Mechanobiol. 1 (1) (2002) 45–57.
[9] Paolo P. Provenzano, Roderic S. Lakes, Thomas Keenan, Ray Vanderby, Nonlinear ligament viscoelasticity, Ann. Biomed. Eng. 29 (10) (2001) 908–914.
[10] Gail M. Thornton, A. Oliynyk, Cyril B. Frank, Nigel G. Shrive, Ligament creep cannot be predicted from stress relaxation at low stress: a biomechanical study of the rabbit medial collateral ligament, J. Orthop. Res. 15 (5) (1997) 652–656.
[11] Kevin L. Troyer, Christian M. Puttlitz, Human cervical spine ligaments exhibit fully nonlinear viscoelastic behavior, Acta Biomater. 7 (2) (2011) 700–709.
[12] Allen C. Pipkin, Tryfan G. Rogers, A non-linear integral representation for viscoelastic behaviour, J. Mech. Phys. Solids 16 (1) (1968) 59–72.
[13] Albert E. Green, Ronald S. Rivlin, The mechanics of non-linear materials with memory - Part I, Arch. Ration. Mech. Anal. 4 (1) (1957) 387–404.
[14] Richard A. Schapery, A theory of nonlinear thermoviscoelasticity based on irreversible thermodynamics, in: Proc. 5th U.S. Nat. Cong. Appl. Mech., ASME, 1966, pp. 511–530.
[15] F. John Lockett, Creep and stress-relaxation experiments for non-linear materials, Int. J. Eng. Sci. 3 (1) (1965) 59–75.
[16] F. John Lockett, Stan Turner, Nonlinear creep of plastics, J. Mech. Phys. Solids 19 (4) (1971) 201–214.
[17] Mario H. Gradowczyk, On the accuracy of the Green-Rivlin representation for viscoelastic materials, Int. J. Solids Struct. 5 (8) (1969) 873–877.
[18] Yuan-Cheng Fung, Biomechanics - Mechanical Properties of Living Tissues, Springer New York, New York, NY, 1981.
[19] Montgomery T. Shaw, William J. MacKnight, Introduction to Polymer Viscoelasticity, John Wiley & Sons Inc., Hoboken, NJ, USA, 2005.
[20] Brad L. Boyce, Reese E. Jones, Thao D. Nguyen, John.M. Grazier, Stress-controlled viscoelastic tensile response of bovine cornea, J. Biomech. 40 (11) (2007) 2367–2376.
[21] Corina S. Drapaca, Giuseppe Tenti, Katrin Rohlf, Sivabal Sivaloganathan, A quasi-linear viscoelastic constitutive equation for the brain: application to hydrocephalus, J. Elast. 85 (1) (2006) 65–83.
[22] Sarah E. Duenwald, Ray Vanderby, Roderic S. Lakes, Constitutive equations for ligament and other soft tissue: evaluation by experiment, Acta Mech. 205 (1–4) (2009) 23–33.
[23] James R. Funk, Gregory W. Hall, Jeff R. Crandall, Walter D. Pilkey, Linear and quasi-linear viscoelastic characterization of ankle ligaments, J. Biomech. Eng. 122 (1) (2000) 15–22.
[24] Roger C. Haut, Robert W. Little, A constitutive equation for collagen fibers, J. Biomech. 5 (5) (1972) 423–430.
[25] Rittu V. Hingorani, Paolo P. Provenzano, Roderic S. Lakes, Anthony Escarcega, Ray Vanderby, Nonlinear viscoelasticity in rabbit medial collateral ligament, Ann. Biomed. Eng. 32 (2) (2004) 306–312.
[26] Jacques M. Huyghe, Dick H. van Campen, Theo Arts, Robert M. Heethaar, The constitutive behaviour of passive heart muscle tissue: a quasi-linear viscoelastic formulation, J. Biomech. 24 (9) (1991) 841–849.
[27] Ali Nekouzadeh, Kenneth M. Pryse, Elliot L. Elson, Guy M. Genin, A simplified approach to quasi-linear viscoelastic modeling, J. Biomech. 40 (14) (2007) 3070–3078.
[28] Michael A. Puso, Jeffrey.A. Weiss, Finite element implementation of anisotropic quasi-linear viscoelasticity using a discrete spectrum approximation, J. Biomech. Eng. 120 (1) (1998) 62–70.
[29] Ariel Sverdlik, Yoram Lanir, Time-dependent mechanical behavior of sheep digital tendons, including the effects of preconditioning, J. Biomech. Eng. 124 (1) (2002) 78–84.
[30] Savio L.-Y. Woo, Bruce R. Simon, Steven C. Kuei, Wayne H. Akeson, Quasi-linear viscoelastic properties of normal articular cartilage, J. Biomech. Eng. 102 (2) (1980) 85–90.
[31] Juan C. Simo, On a fully three-dimensional finite-strain viscoelastic damage model: formulation and computational aspects, Comput. Methods Appl. Mech. Eng. 60 (2) (1987) 153–173.
[32] Gerhard A. Holzapfel, Nonlinear Solid Mechanics: a Continuum Approach for Engineering, John Wiley & Sons Ltd., 2000.
[33] Sanjay Govindjee, Stefanie Reese, A presentation and comparison of two large deformation viscoelasticity models, J. Eng. Mater. Technol. 119 (3) (1997) 251–255.
[34] Harold Berjamin, Michel Destrade, William J. Parnell, On the thermodynamic consistency of quasi-linear viscoelastic models for soft solids, Mech. Res. Commun. 111 (2021) 103648.
[35] Nidhal Jridi, Makrem Arfaoui, Adel Hamdi, Michelle Salvia, Olivier Bareille, Mohamed Ichchou, Jalel Ben Abdallah, Separable finite viscoelasticity: integral-based models vs. experiments, Mech. Time-Depend. Mater. 23 (3) (2019) 295–325.
[36] Estefanía Peña, Juan A. Peña, Manuel Doblaré, On modelling nonlinear viscoelastic effects in ligaments, J. Biomech. 41 (12) (2008) 2659–2666.
[37] Begoña Calvo, Marta Sierra, Jorge Grasa, María J. Muñoz, Estefanía Peña, Determination of passive viscoelastic response of the abdominal muscle and related constitutive modeling: stress-relaxation behavior, J. Mech. Behav. Biomed. Mater. 36 (2014) 47–58.
[38] José M. Benítez, Francisco J. Montáns, The mechanical behavior of skin: structures and models for the finite element analysis, Comput. Struct. 190 (2017) 75–107.
[39] T. Christian Gasser, Caroline Forsell, The numerical implementation of invariant-based viscoelastic formulations at finite strains. An anisotropic model for the passive myocardium, Comput. Methods Appl. Mech. Eng. 200 (49–52) (2011) 3637–3645.
[40] Gerhard A. Holzapfel, T. Christian Gasser, Michael Stadler, A structural model for the viscoelastic behavior of arterial walls: continuum formulation and finite element analysis, Eur. J. Mech. A, Solids 21 (3) (2002) 441–463.
[41] Michael Kaliske, Heinrich Rothert, Formulation and implementation of three-dimensional viscoelasticity at small and finite strains, Comput. Mech. 19 (3) (1997) 228–239.
[42] Estefanía Peña, Begoña Calvo, Miguel A. Martínez, Manuel Doblaré, An anisotropic visco-hyperelastic model for ligaments at finite strains. Formulation and computational aspects, Int. J. Solids Struct. 44 (3–4) (2007) 760–778.
[43] Stefanie Reese, Sanjay Govindjee, A theory of finite viscoelasticity and numerical aspects, Int. J. Solids Struct. 35 (26–27) (1998) 3455–3482.
[44] Francois Sidoroff, Un modele viscoelastique non lineaire avec configuration intermediaire, J. Méc. 13 (4) (1974) 679–713.

[45] Dal Hüsnü, Michael Kaliske, Bergström–Boyce model for nonlinear finite rubber viscoelasticity: theoretical aspects and algorithmic treatment for the FE method, Comput. Mech. 44 (6) (2009) 809–823.
[46] Tobias Scheffer, Florian Goldschmidt, Stefan Diebels, Implementation of the strongly pronounced non-linear viscoelasticity of an incompressible filled rubber, Tech. Mech. 35 (2) (2015) 118–132.
[47] Michelle S. Hoo Fatt, Xin Ouyang, Three-dimensional constitutive equations for styrene butadiene rubber at high strain rates, Mech. Mater. 40 (1–2) (2008) 1–16.
[48] Thao D. Nguyen, Reese E. Jones, Brad L. Boyce, Modeling the anisotropic finite-deformation viscoelastic behavior of soft fiber-reinforced composites, Int. J. Solids Struct. 44 (25–26) (2007) 8366–8389.
[49] Hongliang Liu, Gerhard A. Holzapfel, Bjørn H. Skallerud, Victorien Prot, Anisotropic finite strain viscoelasticity: constitutive modeling and finite element implementation, J. Mech. Phys. Solids 124 (2019) 172–188.
[50] Marcos Latorre, Francisco J. Montáns, Strain-level dependent nonequilibrium anisotropic viscoelasticity: application to the abdominal muscle, J. Biomech. Eng. 139 (10) (2017) 1–9.
[51] Satish K. Panda, Martin L. Buist, A finite nonlinear hyper-viscoelastic model for soft biological tissues, J. Biomech. 69 (2018) 121–128.
[52] Jeffrey E. Bischoff, Ellen M. Arruda, Karl Grosh, A rheological network model for the continuum anisotropic and viscoelastic behavior of soft tissue, Biomech. Model. Mechanobiol. 3 (1) (2004) 56–65.
[53] Marcos Latorre, Francisco J. Montáns, Anisotropic finite strain viscoelasticity based on the Sidoroff multiplicative decomposition and logarithmic strains, Comput. Mech. 56 (3) (2015) 503–531.
[54] Silvia Budday, Gerhard Sommer, Johannes Haybaeck, Paul Steinmann, Gerhard A. Holzapfel, Ellen Kuhl, Rheological characterization of human brain tissue, Acta Biomater. 60 (2017) 315–329.
[55] Karl A. Kalina, Lennart Linden, Jörg Brummund, Markus Kästner, FE^{ANN}: an efficient data-driven multiscale approach based on physics-constrained neural networks and automated data mining, Comput. Mech. 71 (5) (2023) 827–851.
[56] Dominik K. Klein, Rogelio Ortigosa, Jesús Martínez-Frutos, Oliver Weeger, Finite electro-elasticity with physics-augmented neural networks, Comput. Methods Appl. Mech. Eng. 400 (2022) 115501.
[57] Alexander Hartmaier, Data-oriented constitutive modeling of plasticity in metals, Materials 13 (7) (2020) 1600.
[58] Georgios Kissas, Yibo Yang, Eileen Hwuang, Walter R. Witschey, John A. Detre, Paris Perdikaris, Machine learning in cardiovascular flows modeling: predicting arterial blood pressure from non-invasive 4D flow MRI data using physics-informed neural networks, Comput. Methods Appl. Mech. Eng. 358 (January) (2020) 112623.
[59] Mauricio Fernández, Shahed Rezaei, Jaber Rezaei Mianroodi, Felix Fritzen, Stefanie Reese, Application of artificial neural networks for the prediction of interface mechanics: a study on grain boundary constitutive behavior, Adv. Model. Simul. Eng. Sci. 7 (1) (2020).
[60] Mauricio Fernández, Felix Fritzen, Oliver Weeger, Material modeling for parametric, anisotropic finite strain hyperelasticity based on machine learning with application in optimization of metamaterials, Int. J. Numer. Methods Eng. 123 (2) (2022) 577–609.
[61] Markus Oeser, Steffen Freitag, Modeling of materials with fading memory using neural networks, Int. J. Numer. Methods Eng. 78 (7) (2009) 843–862.
[62] Steffen Freitag, Wolfgang Graf, Michael Kaliske, A material description based on recurrent neural networks for fuzzy data and its application within the finite element method, Comput. Struct. 124 (2013) 29–37.
[63] Christoph Zopf, Michael Kaliske, Numerical characterisation of uncured elastomers by a neural network based approach, Comput. Struct. 182 (2017) 504–525.
[64] Guang Chen, Recurrent neural networks (RNNs) learn the constitutive law of viscoelasticity, Comput. Mech. 67 (3) (2021) 1009–1019.
[65] Clifford Truesdell, Walter Noll, The non-linear field theories of mechanics, in: The Non-Linear Field Theories of Mechanics, Springer, Berlin, Heidelberg, 2004, pp. 1–579.
[66] Benoit Jordan, Maysam B. Gorji, Dirk Mohr, Neural network model describing the temperature- and rate-dependent stress-strain response of polypropylene, Int. J. Plast. 135 (2020) 102811.
[67] Enzo Marino, Moritz Flaschel, Siddhant Kumar, Laura De Lorenzis, Automated identification of linear viscoelastic constitutive laws with EUCLID, Mech. Mater. 181 (2023) 104643.
[68] Kevin Linka, Nina Reiter, Jasmin Würges, Martin Schicht, Lars Bräuer, Christian J. Cyron, Friedrich Paulsen, Silvia Budday, Unraveling the local relation between tissue composition and human brain mechanics through machine learning, Front. Bioeng. Biotechnol. 9 (2021) 704738.
[69] Trenton Kirchdoerfer, Michael Ortiz, Data-driven computational mechanics, Comput. Methods Appl. Mech. Eng. 304 (2016) 81–101.
[70] Robert Eggersmann, Trenton Kirchdoerfer, Stefanie Reese, Laurent Stainier, Michael Ortiz, Model-free data-driven inelasticity, Comput. Methods Appl. Mech. Eng. 350 (2019) 81–99.
[71] Hossein Salahshoor, Michael Ortiz, Model-free data-driven viscoelasticity in the frequency domain, Comput. Methods Appl. Mech. Eng. 403 (2023) 115657.
[72] Kevin Linka, Markus Hillgärtner, Kian P. Abdolazizi, Roland C. Aydin, Mikhail Itskov, Christian J. Cyron, Constitutive artificial neural networks: a fast and general approach to predictive data-driven constitutive modeling by deep learning, J. Comput. Phys. 429 (2021) 110010.
[73] Alexander E. Ehret, Mikhail Itskov, A polyconvex hyperelastic model for fiber-reinforced materials in application to soft tissues, J. Mater. Sci. 42 (21) (2007) 8853–8863.
[74] Yavuz Başar, Dieter Weichert, Nonlinear Continuum Mechanics of Solids, Springer, Berlin, Heidelberg, 2000.
[75] Ray W. Ogden, Nonlinear Elastic Deformations, Dover Publications, 1997.
[76] Jin Min Zhang, Jan Rychlewski, Structure tensors for anisotropic solids, Arch. Mech. 42 (3) (1990) 267–277.
[77] Itskov Mikhail, Tensor Algebra and Tensor Analysis for Engineers, Springer, Berlin, Heidelberg, 2009.
[78] Jean-Paul Boehler, On irreducible representations for isotropic scalar functions, Z. Angew. Math. Mech. 57 (6) (1977) 323–327.
[79] John M. Ball, Convexity conditions and existence theorems in nonlinear elasticity, Arch. Ration. Mech. Anal. 63 (4) (1976) 337–403.
[80] Mokarram Hossain, Rukshan Navaratne, Djordje Perić, 3D printed elastomeric polyurethane: viscoelastic experimental characterizations and constitutive modelling with nonlinear viscosity functions, Int. J. Non-Linear Mech. 126 (2020) 103546.
[81] Juan C. Simo, Thomas J.R. Hughes, Computational Inelasticity, Interdisciplinary Applied Mathematics, vol. 7, Springer-Verlag, New York, 1998.
[82] Corina S. Drapaca, Sivabal Sivaloganathan, Giuseppe Tenti, Nonlinear constitutive laws in viscoelasticity, Math. Mech. Solids 12 (5) (2007) 475–501.
[83] Brandon Amos, Lei Xu, J. Zico Kolter, Input convex neural networks, in: Proceedings of the 34th International Conference on Machine Learning, PMLR, 2017.
[84] Stephen P. Boyd, Lieven Vandenberghe, Convex Optimization, Cambridge University Press, 2004.
[85] Stefan Hartmann, Patrizio Neff, Polyconvexity of generalized polynomial-type hyperelastic strain energy functions for near-incompressibility, Int. J. Solids Struct. 40 (11) (2003) 2767–2791.
[86] Jörg Schröder, Patrizio Neff, Invariant formulation of hyperelastic transverse isotropy based on polyconvex free energy functions, Int. J. Solids Struct. 40 (2) (2003) 401–445.
[87] Daniel Balzani, Patrizio Neff, Jörg Schröder, Gerhard A. Holzapfel, A polyconvex framework for soft biological tissues. Adjustment to experimental data, Int. J. Solids Struct. 43 (20) (2006) 6052–6070.
[88] Roderic S. Lakes, Viscoelastic Materials, Cambridge University Press, 2009.
[89] Dimitri Jalocha, Andrei Constantinescu, Robert Neviere, Revisiting the identification of generalized Maxwell models from experimental results, Int. J. Solids Struct. 67–68 (2015) 169–181.
[90] Prateek Sharma, Anna K. Sambale, Markus Stommel, Michael Maisl, Hans-Georg Herrmann, Stefan Diebels, Moisture transport in PA6 and its influence on the mechanical properties, Contin. Mech. Thermodyn. 32 (2) (2020) 307–325.

[91] Julie Diani, Pierre Gilormini, Carole Frédy, Ingrid Rousseau, Predicting thermal shape memory of crosslinked polymer networks from linear viscoelasticity, Int. J. Solids Struct. 49 (5) (2012) 793–799.
[92] Michael Baumgaertel, H. Henning Winter, Determination of relaxation and retardation spectra from dynamical mechanical data, Rheol. Acta 28 (1989) 511–519.
[93] Michael Baumgaertel, H. Henning Winter, Interrelation between continuous and discrete time spectra, J. Non-Newton. Fluid Mech. 44 (1992) 15–36.
[94] Rebecca Rothermel, Wladimir Panfilenko, Prateek Sharma, Anne Wald, Thomas Schuster, Anne Jung, Stefan Diebels, A method for determining the parameters in a rheological model for viscoelastic materials by minimizing Tikhonov functionals, Appl. Math. Sci. Eng. 30 (1) (2022) 141–165.
[95] Andrey N. Tikhonov, Vasiliy Y. Arsenin, Solutions of Ill-Posed Problems, V. H. Winston & Sons, Washington, D.C., 1977.
[96] François Chollet, Keras, 2015.
[97] Martín Abadi, Paul Barham, Jianmin Chen, Zhifeng Chen, Andy Davis, Jeffrey Dean, Matthieu Devin, Sanjay Ghemawat, Geoffrey Irving, Michael Isard, Manjunath Kudlur, Josh Levenberg, Rajat Monga, Sherry Moore, Derek G. Murray, Benoit Steiner, Paul Tucker, Vijay Vasudevan, Pete Warden, Martin Wicke, Yuan Yu, Xiaoqiang Zheng, TensorFlow: a system for large-scale machine learning, in: Proceedings of the 12th USENIX Symposium on Operating Systems Design and Implementation, OSDI 2016, 2016, pp. 265–283.
[98] Ray W. Ogden, Large deformation isotropic elasticity – on the correlation of theory and experiment for incompressible rubberlike solids, Proc. R. Soc. Lond. Ser. A, Math. Phys. Sci. 326 (1567) (1972) 565–584.
[99] Gerhard A. Holzapfel, T. Christian Gasser, Ray W. Ogden, A new constitutive framework for arterial wall mechanics and a comparative study of material models, J. Elast. 61 (1–3) (2000) 1–48.
[100] Mokarram Hossain, Duc Khoi Vu, Paul Steinmann, Experimental study and numerical modelling of VHB 4910 polymer, Comput. Mater. Sci. 59 (2012) 65–74.
[101] Ellen M. Arruda, Mary C. Boyce, A three-dimensional constitutive model for the large stretch behavior of rubber elastic materials, J. Mech. Phys. Solids 41 (2) (1993) 389–412.
[102] Christian Linder, Mykola Tkachuk, Christian Miehe, A micromechanically motivated diffusion-based transient network model and its incorporation into finite rubber viscoelasticity, J. Mech. Phys. Solids 59 (10) (2011) 2134–2156.
[103] Jianyou Zhou, Liying Jiang, Roger E. Khayat, A micro–macro constitutive model for finite-deformation viscoelasticity of elastomers with nonlinear viscosity, J. Mech. Phys. Solids 110 (2018) 137–154.
[104] Paolo Del Linz, Yi Wang, Paul A. Hooper, Hari Arora, David Smith, Luke Pascoe, David Cormie, Bamber R.K. Blackman, John P. Dear, Determining material response for polyvinyl butyral (PVB) in blast loading situations, Exp. Mech. 56 (9) (2016) 1501–1517.
[105] Zisheng Liao, Mokarram Hossain, Xiaohu Yao, Markus Mehnert, Paul Steinmann, On thermo-viscoelastic experimental characterization and numerical modelling of VHB polymer, Int. J. Non-Linear Mech. 118 (2020) 103263.
[106] T. Christian Gasser, Ray W. Ogden, Gerhard A. Holzapfel, Hyperelastic modelling of arterial layers with distributed collagen fibre orientations, J. R. Soc. Interface 3 (6) (2006) 15–35.
[107] Gerhard A. Holzapfel, On large strain viscoelasticity: continuum formulation and finite element applications to elastomeric structures, Int. J. Numer. Methods Eng. 39 (22) (1996) 3903–3926.
[108] Kevin Linka, Ellen Kuhl, A new family of constitutive artificial neural networks towards automated model discovery, Comput. Methods Appl. Mech. Eng. 403 (jan 2023) 115731.